

Accepted for publication in the Astronomical Journal

Exploring the Interstellar Media of Optically Compact Dwarf Galaxies

Hans P. Most, John M. Cannon

Department of Physics & Astronomy, Macalester College, 1600 Grand Avenue, Saint Paul, MN 55105

`hmost@macalester.edu, jcannon@macalester.edu`

John J. Salzer

Department of Astronomy, Indiana University, 727 East Third Street, Bloomington, IN 47405

`slaz@astro.indiana.edu`

Jessica L. Rosenberg

School of Physics, Astronomy, and Computational Science, George Mason University, Fairfax, VA 22030

`jrosenb4@gmu.edu`

Eric Engstrom

Department of Physics & Astronomy, Macalester College, 1600 Grand Avenue, Saint Paul, MN 55105

Palmer Fliss

Department of Physics & Astronomy, Macalester College, 1600 Grand Avenue, Saint Paul, MN 55105

Department of Earth Sciences, University of Minnesota, Minneapolis, MN, 55455

ABSTRACT

We present new *Very Large Array* H I spectral line, archival *Sloan Digital Sky Survey*, and archival *Spitzer Space Telescope* imaging of eight star-forming

blue compact dwarf galaxies that were selected to be optically compact (optical radii <1 kpc). These systems have faint blue absolute magnitudes ($M_B \gtrsim -17$), ongoing star formation (based on emission-line selection by the $H\alpha$ or $[O\ III]$ lines), and are nearby (mean velocity = $3315\text{ km s}^{-1} \simeq 45$ Mpc). One galaxy in the sample, ADBS 113845+2008, is found to have an $H\text{ I}$ halo that extends 58 r-band scale lengths from its stellar body. In contrast, the rest of the sample galaxies have $H\text{ I}$ radii to optical-scale-length ratios ranging from 9.3 to 26. The size of the $H\text{ I}$ disk in the “giant disk” dwarf galaxy ADBS 113845+2008 appears to be unusual as compared to similarly compact stellar populations.

Subject headings: galaxies: evolution — galaxies: dwarf — galaxies: irregular — galaxies: individual (IC 2271, ADBS 113845+2008, KISSR 245, KISSR 278, KISSR 396, KISSR 561, KISSR 572, KISSR 1021)

1. Introduction

Blue compact dwarf galaxies (hereafter, BCDs) have emerged as a particularly intriguing subset of dwarf galaxies that have been studied in the local universe ($z \lesssim 0.05$). Since the early studies and characterizations by Thuan & Martin (1981) and Thuan (1983), many investigations have classified BCDs as systems that harbor spatially and temporally concentrated ongoing star formation in a low-mass galaxy potential well. While definitions in the literature vary, BCDs are intrinsically faint systems ($M_B \gtrsim -17$) that exhibit ongoing star formation over the bulk of an otherwise physically compact stellar population.

Detailed studies of individual, nearby BCDs have provided important insights into their physical properties and into the mechanisms that initiate and govern their star formation. van Zee et al. (1998) found that five compact dwarf galaxies that are currently experiencing strong bursts of star formation exhibit central $H\text{ I}$ surface densities that are significantly higher than those of dwarf irregular (dIrr) galaxies. Similarly, some well-studied BCDs harbor very high column density neutral hydrogen gas in the regions of active star formation (e.g., $N_{HI} \simeq 2.4 \times 10^{22}\text{ cm}^{-2}$ in I Zw 18; see Brown et al. 2002 and van Zee et al. 2006). Other recent studies have verified that many nearby and well-resolved systems have high neutral gas surface densities in the regions of ongoing star formation (see, e.g., Thuan et al. 2004, Elson et al. 2010, and references therein).

The physical mechanism(s) that create this central concentration of neutral gas remain(s) ambiguous. One commonly proposed solution is that the current burst events in BCDs are the result of a gravitational interaction with a nearby companion (e.g., Östlin et al.

2001). While there are examples of apparently interaction-driven burst events (e.g., the SBS 1129+576 system studied by Ekta et al. 2006), there are also systems that have been shown to be quite isolated (see, for example, van Zee et al. 1998, Bureau et al. 1999, and further discussion below). While undiscovered, very low-mass companions may reside near some of these isolated systems (consider, for example, the discovery of an interaction with a low surface brightness companion to the Magellanic irregular NGC 4449 by Martínez-Delgado et al. 2012), the gravitational interaction trigger does not appear to be universal in BCD galaxies. The origin of the concentrated star formation in at least some of the isolated BCDs appears to require a different initiation mechanism.

While the properties of isolated BCDs have been studied in some detail (e.g., the studies of NGC 2915 by Meurer et al. 1994, 1996), a particularly intriguing system was discovered in the *Arecibo Dual Beam Survey* (ADBS) by Rosenberg & Schneider (2000, 2002): ADBS 113845+2008. This galaxy was subsequently cataloged as a UV-excess source in the 2nd KISO survey (Miyauchi-Isobe & Maehara, 2000). Its extremely compact nature was first recognized during *WIYN* 0.9-meter¹ broadband imaging of selected ADBS galaxies. The optical component was found to be extremely compact (B-band exponential scale length = 0.57 kpc); H α narrowband imaging confirmed a high ongoing star formation rate ($0.06 \text{ M}_{\odot} \text{ yr}^{-1}$) within this optically compact stellar component.

Subsequent *Very Large Array*² (*VLA*) H I spectral line imaging of the source revealed that the neutral gas disk was extremely extended compared to the compact optical structure. As discussed in detail in Cannon et al. (2009), H I gas was detected to a maximum radial distance of ~ 25 kpc at the 10^{19} cm^{-2} level; it thus possesses one of the largest H I-to-optical size ratios of any known dwarf galaxy. In contrast to some detailed H I studies of other BCD systems that have found complex velocity structure (e.g., van Zee et al. 1998; Simpson et al. 2011), ADBS 113845+2008 is undergoing well-ordered rotation throughout most of the neutral gas disk.

Perhaps the most mysterious quality of ADBS 113845+2008 is that its neutral gas morphology is dominated by a broken ring structure that is roughly 15 kpc in diameter. This ring contains the highest column density neutral gas in the galaxy and is not coincident

¹The *WIYN* 0.9-meter telescope is operated jointly by a consortium that includes Indiana University, San Francisco State University, the University of Wisconsin-Madison, the University of Wisconsin-Stevens Point, the University of Wisconsin-Whitewater, Austin Peay State University, Haverford College, the Rochester Institute of Technology, and the Wisconsin Space Grant Consortium.

²The National Radio Astronomy Observatory is a facility of the National Science Foundation operated under cooperative agreement by Associated Universities, Inc.

with the optical component. Rather, the star-forming component resides in a relative H I under-density. Cannon et al. (2009) interpret this result to be a signature of an extremely inefficient mode of star formation in a very isolated galaxy. We hereafter refer to this striking collection of physical properties as the “giant disk” phenomenon in dwarf galaxies.

The remarkable characteristics of ADBS 113845+2008 are the origin of the present investigation. Stated most simply, we seek to understand if this “giant disk” scenario is common or rare in star-forming dwarf galaxies that have stellar components that are as strongly centrally concentrated as the one in ADBS 113845+2008. To this end, we present new optical, infrared, and H I imaging of a sample of extremely optically compact dwarf galaxies. The new observations presented here confirm the rarity of the “giant disk” found in the ADBS 113845+2008 system.

2. Observations and Data Reduction

2.1. Survey Selection Criteria

The sample of optically compact galaxies studied in this paper was produced using specific selection criteria designed to identify star-forming galaxies with compact stellar components; ADBS 113845+2008 and IC 2271 were already known to have such characteristics from previous imaging. Starting with the full *KPNO International Spectroscopic Survey* (*KISS*, an objective-prism survey for extragalactic emission-line objects; Salzer et al. 2000, 2001, 2002) database, we searched for emission-line objects that were spectroscopically-confirmed. To maximize physical resolution an upper velocity constraint was set at $V_{\text{sys}} < 5,000 \text{ km s}^{-1}$. Photometric parameters were obtained for these objects from the *SDSS* using the *SkyTools*³ interface. Objects with optical radii less than $3''$ were selected; these were then individually inspected to ensure a compact optical structure. Finally, we searched for archival single-dish H I observations of these remaining systems in order to determine their suitability for *VLA* observing. This resulted in a sample of six galaxies selected from the *KISS* catalogs. We stress that this sample is meant to be representative of the compact dwarf class, but it is not complete in the sense of being a volume-limited sample of such sources.

All of these galaxies share the following characteristics: 1) optical compactness (optical radii at 50% peak brightness of $\lesssim 1 \text{ kpc}$); 2) faint blue absolute magnitudes ($M_B \gtrsim -17$); 3) ongoing star formation (based on emission-line selection by the $\text{H}\alpha$ or $[\text{O III}]$ lines); and 4) proximity for spatially resolved work with the *VLA* C-array ($15''$ beam $\lesssim 5 \text{ kpc}$ for all systems;

³See <http://cas.sdss.org/astro/en/tools/crossid/upload.asp>

mean velocity = $3315 \text{ km s}^{-1} \simeq 45 \text{ Mpc}$). Note that in the work of Cannon et al. (2009), ADBS 113845+2008 was selected using these same criteria. It is important to emphasize that the six *KISS* galaxies in the present study (see Table 1 for salient properties) were selected based on their optical properties alone; the H I flux integrals were used only to determine observational feasibility.

2.2. VLA H I Spectral Line Observations

H I spectral line imaging of each of the sample galaxies was obtained with the *VLA* in the C configuration via observing programs AC 841 and AC 919 (PI: Cannon). The *VLA* correlator was used in a standard single polarization mode, providing 64 or 128 channels over a 1.56 or 3.12 MHz bandwidth. The velocity resolution ($2.56, 5.15$, or $10.3 \text{ km s}^{-1} \text{ ch}^{-1}$) was selected based on the (single dish) line width of each source. Combinations of bandwidth and frequency resolution were selected to guarantee sufficient line-free channels to allow an accurate removal of the continuum emission. Table 2 provides details about each observing session from which data are presented in this work.

All reductions were performed using the Astronomical Image Processing (AIPS) package. Due to the array being in a “hybrid” state, containing both *VLA* and *EVLA* receivers, standard reduction procedures were followed with necessary modifications to account for the “aliasing” effect that arose due to the digital-to-analog conversion required to correlate *EVLA* signals using the old *VLA* correlator. This effect was most egregious for narrow bandwidth observations. We thus followed the NRAO instructions of flagging *EVLA-EVLA* baselines before and unflagging them after the tasks BPASS and CALIB⁴. The resulting continuum subtraction was performed using a first-order fit in UVLSF to channels where the bandpass was demonstrably flat. We found no measurable differences between this calibration approach and one where we disregarded the *EVLA* antennas completely and followed standard reduction procedures. We note that there were only 5 *EVLA* antennas in the array during the C configuration observation of ADBS 113845+2008 (which would contain the most measurable aliasing effect, given the bandwidths listed in Table 2).

Two data cubes were produced for each galaxy using the task IMAGR and each one was cleaned to 2 times the rms noise (Högbom 1974; Clark 1980). First, “low-resolution” cubes were created using natural weighting (ROBUST = 5 in the AIPS IMAGR task). These cubes were convolved to a circular beam size of $20'' \times 20''$. Second, “high-resolution” cubes were created using robust weighting (ROBUST = 0.5; see Briggs 1995). These cubes were

⁴See <https://science.nrao.edu/facilities/vla/obsolete/aliasing> for more details

convolved to a circular beam size of $15'' \times 15''$.

To create blanked cubes and moment maps, the naturally weighted cubes were convolved to a beam size of $30''$. These cubes were blanked at the 2σ level found in line-free channels. The cubes were then inspected by hand, and emission in three or more consecutive channels was considered to be real. These cubes were then used to blank both the “low-” ($20''$) and “high-resolution” ($15''$) cubes. Through this procedure, we assure that the same pixels contribute to both the “low-” and the “high-resolution” cubes. Moment maps showing integrated H I emission and velocity structures were created using the techniques discussed in detail in Cannon et al. (2009).

As seen in Table 3, the total H I flux integrals derived for the sample galaxies are each lower than the *Arecibo Observatory* single dish observations (Rosenberg & Schneider 2000, 2002; Lee et al. 2002). The cause of these differences is at least partly due to the missing short uv spacings of the *VLA* compared to a single dish measurement. For example, the observed H I flux integral of IC 2271 of $1.22 \text{ Jy km s}^{-1}$ is significantly lower than the value found by Rosenberg & Schneider (2000) using the *VLA* D array (4.7 Jy km s^{-1}). Similarly, the total H I flux integral derived for ADBS 113845+2008 ($1.58 \text{ Jy km s}^{-1}$) is lower than the $2.58 \text{ Jy km s}^{-1}$ found by Cannon et al. (2009) using combined C and D configuration data. A re-reduction of the D configuration data sets as part of the present analysis confirms a higher flux integral using the more compact configuration ($S_{\text{HI}} = 2.12 \pm 0.21 \text{ Jy km s}^{-1}$ for ADBS 113845+2008 and $S_{\text{HI}} = 1.61 \pm 0.16 \text{ Jy km s}^{-1}$ for IC 2271, both with $55''$ circular beam sizes). Since the KISSR galaxies (which constitute the bulk of the present sample) have only C configuration observations, we chose to intentionally omit the D configuration data for IC 2271 and ADBS 113845+2008 from the present analysis; this assures that all eight galaxies have similar thresholds for surface brightness sensitivity at different spatial scales.

In an effort to recover as much flux from each of the target galaxies as possible, we performed various tests with the *VLA* uv datasets. Long baselines were downweighted in IMAGR via tapering in the uv plane. Circular beam size cubes with resolution elements of $15''$, $30''$, and $60''$ were created for each galaxy using appropriate UVTAPER values. The results of these tests are summarized in Table 4. There are only modest gains in the recovered flux integrals for most sources. KISSR 278 shows the most pronounced increase in S_{HI} when moving from $15''$ to $30''$ resolution. Note that IC 2271 and ADBS 113845+2008, which have the largest single dish flux integrals (see Table 3), show only modest increases in S_{HI} when downweighting long baselines. This is strong evidence that the missing shortest spacing baselines are important for the recovery of all of the H I flux from these systems.

We also experimented with calibrating our uv data using only certain baselines in the

array. Using KISSR 561 as a template, we independently calibrated the uv data in five different ways: by removing the *VLA-EVLA* baselines; by removing the *VLA-VLA* baselines; by retaining only the *EVLA-EVLA* baselines; by retaining only the *VLA-VLA* baselines; and by the previously discussed method in which the *EVLA-EVLA* baselines were flagged and unflagged around specific tasks. We find no significant differences in the galaxy’s morphology amongst these tests. The last method (i.e., the flagging and unflagging of *EVLA-EVLA* baselines) proved to recover the most flux, and so was used for all datasets in the sample.

As we discuss in detail in § 3.2 below, five of the eight sample galaxies have nearby companions, some of which are very H I-bright. A third possible explanation for the lower flux integrals derived for some of the systems studied here is that these high-surface-brightness companions introduce sidelobes, the imperfect cleaning of which will prevent a full recovery of the flux integral from the dim target galaxies. In fact, this effect can lead to the single dish flux measurements being erroneously high. The system that is most egregiously affected in this way is KISSR 396; as we discuss below, this source is a companion to the massive spiral NGC 5375. It is possible that the single dish measurement of KISSR 396 is an over-estimate, since NGC 5375 is in the first sidelobe of the single-dish primary beam. In an attempt to image this complex field with high fidelity, we implemented cleaning algorithms using both multi-faceted cleans around the detected galaxies and multi-scale clean algorithms (Cornwell 2008). Neither approach produced significant increases in the flux integral recovered from KISSR 396. We thus use the *VLA* S_{HI} values quoted in Table 3 throughout the remainder of this work.

2.3. *SDSS* and *Spitzer* Observations

Optical and infrared imaging of the sample galaxies was obtained from public archival databases to facilitate detailed comparisons with the H I imaging presented here. This was necessary because the imaging data obtained as part of *KISS* (Salzer et al. 2000, 2001) had an image scale of $2.0'' \text{ pixel}^{-1}$; none of the *KISS* galaxies studied here are resolved in the survey data. Optical r-band images were obtained from the *SDSS* Data Release Eight (Aihara et al. 2011). $3.6 \mu\text{m}$ and $4.5 \mu\text{m}$ *Spitzer* images of the six KISSR galaxies were obtained from the *Spitzer Heritage Archive* (*Spitzer* imaging of IC 2271 and ADBS 113845+2008 is not available). No further treatments of the pipeline-processed archival data were required. These images are discussed in further detail in the sections below.

Throughout this paper we will discuss the physical sizes of the galaxies in this sample. We thus draw specific attention to the angular resolution of the optical and infrared imaging used in our analysis. The FWHM of the *Spitzer*/IRAC images is $1.66''$ at $3.6 \mu\text{m}$ and $1.72''$ at

$4.5 \mu\text{m}^5$. Similarly, the median PSF FWHM of *SDSS* r-band images is quoted as $1.3''^6$, and we adopt this value here; using the individual images we analyze in this work, we measure empirical PSF FWHM values ranging from $0.94''$ (IC 2271) to $1.22''$ (KISSR 245).

3. H I and Stellar Distributions

3.1. Target Galaxies

Using the blanked datacubes discussed in § 2.2, real emission in each channel was summed in order to create the global H I profiles shown in Figures 1 and 2. It is immediately evident that the neutral gas disks of the sample galaxies span a wide range of physical characteristics. Two systems show broad H I profiles ($\Delta V \gtrsim 100 \text{ km s}^{-1}$) that are indicative of bulk rotation (e.g, ADBS 113845+2008, KISSR 561). Three systems show what may be double-horned or broad profiles that are measured with poor fidelity (e.g., KISSR 245, KISSR 396, KISSR 1021). Three systems show simple single-peak profiles indicative of either low rotation velocities or nearly face-on inclination angles (e.g, IC 2271, KISSR 278, KISSR 572).

The profiles shown in Figures 1 and 2 should be compared with the recovered flux integrals presented in Table 3 and discussed in § 2.2. The three systems with the smallest recovered S_{HI} values in Table 3 (KISSR 278, KISSR 396, KISSR 572) are those systems with the narrowest H I profiles. Note specifically that KISSR 278, KISSR 396, and KISSR 572 are each only detected in 4, 7, and 3 consecutive channels of their datacubes, respectively. It is important to keep the low signal to noise ratio of some of these galaxies in mind during the discussion that follows.

Single dish profiles of the six KISSR galaxies in Figures 1 and 2 were presented in Lee et al. (2002). A comparison of these two sets of profiles shows similar morphologies in some cases; the profiles of KISSR 278, KISSR 396, and KISSR 561 shown in Figures 1 and 2 are similar in shape as those shown in Lee et al. (2002), although with slightly weaker peak flux densities in the interferometric global profiles. Conversely, the other three KISSR systems (KISSR 245, KISSR 572, and KISSR 1021) show significant differences in the shapes of their profiles; the single-dish profiles not only recover more flux (see detailed discussion in § 2.2 above), but they also recover different morphologies (note, for example, that the single dish profile of KISSR 1021 shows a pronounced double-horn morphology that is only poorly

⁵see the IRAC Instrument Handbook at <http://ssc.spitzer.caltech.edu>

⁶www.sdss.org

recovered in the interferometric global profile).

Figures 3 through 10 compare the H I, optical, and infrared (available for six of the eight systems, excluding IC 2271 and ADBS 113845+2008) images of the eight sample galaxies. Using the 2 kpc physical length denoted in panel (b) of each figure, it is immediately evident that the high surface brightness stellar component of each of these eight galaxies is extremely compact. In fact, some of these galaxies are only slightly more extended than foreground stars found in the fields [note the close proximity of foreground stars to ADBS 113845+2008 (Figure 4) and KISSR 561 (Figure 8)]; we discuss the effects of resolution on our results in more detail below. While the H I surface brightness varies from one system to the next, each of these eight galaxies is detected at high significance in both the *SDSS* and in the *Spitzer* images.

An examination of the H I column density images and contours in Figures 3 through 10 reveals that all of the galaxies in this sample, with the exception of ADBS 113845+2008, harbor centrally concentrated neutral gas distributions at these spatial resolutions. In most cases the optical and infrared surface brightness maxima are spatially coincident with the highest detected column density region (e.g., IC 2271 in Figure 3, KISSR 572 in Figure 9); in some systems there is a small offset between these two maxima, but most of these offsets are smaller than the synthesized beam sizes and are thus not significant. The most significant discrepancy between the stellar and gaseous components is found in ADBS 113845+2008: as discussed in detail in Cannon et al. (2009), the H I morphology is dominated by a broken ring structure that surrounds the optical body of the system. The stellar component is many kpc away from the highest column density neutral gas.

Similarly, an examination of the optical and infrared images of these sources reveals that most members of the sample are extremely compact. However, it is important to stress that each of the systems is spatially resolved in the *SDSS* images, the *Spitzer* images, or both; we discuss this in more detail in § 4.1 below. A few of the galaxies do have low surface brightness emission in the optical and infrared that may be indicative of the compact burst being only the highest surface brightness component of a larger stellar disk. The most obvious systems with these properties are KISSR 278 (Figure 6), KISSR 561 (Figure 8, but note that the compact and high surface brightness object in the northern part of the stellar disk is a foreground star), and KISSR 572 (Figure 9).

The images shown in Figures 3 through 10 reveal that five of the eight neutral gas disks extend well beyond the beam size at this sensitivity level; the H I disks of KISSR 278, KISSR 396, and KISSR 572 are the same size as the beam. There are low surface brightness extensions of H I gas in some systems: IC 2271 (Figure 3) and KISSR 1021 (Figure 10) harbor H I disks that are roughly twice the size of the stellar body; KISSR 245 (Figure 5) and

KISSR 561 (Figure 8) show tenuous H I filaments extending toward the southwest. However, the low signal to noise ratio of most of these datasets (see discussion in § 2) precludes a robust kinematic study of seven of the eight systems in this work. The detailed dynamical analysis of ADBS 113845+2008 is already presented in Cannon et al. (2009), to which we refer the interested reader for details and results.

While dynamical analyses are not possible with most of the data presented here, the derived surface densities are robustly measured (at this modest sensitivity level). Stated differently, an analysis of the (projected) surface densities in each system does not require a detailed knowledge of the gas dynamics. We thus limit our interpretation to those qualities and quantities of the neutral gas that do not depend on dynamical properties. We focus on quantifying the relative sizes of the neutral gas and stellar disks, as a measure of the frequency of the “giant disk” phenomenon; most of § 4 is devoted to addressing this science goal.

One such well-studied metric is the empirical relationship between H I column density and ongoing star formation. While we do not have H α imaging of all of these sources, each is a spectroscopically confirmed emission line source from KISS (Salzer et al. 2000, 2001, 2002). We make the implicit assumption that the majority of the ongoing star formation in these systems is spatially coincident with the high surface brightness stellar components shown in the optical images in Figures 3 through 10. We note explicitly that the most extreme member of this sample, ADBS 113845+2008, has an H α morphology that is essentially indistinguishable from that of the r-band image shown in Figure 4 (see, e.g., Figure 5 of Cannon et al. 2009).

A gas column density of 10^{21} cm^{-2} has been shown to trace locations of active star formation (e.g., Skillman 1987; Kennicutt 1989; Kennicutt 1998; and references therein). Interestingly, in all of the galaxies, except IC 2271 and KISSR 561, the peak observed H I column densities are below this 10^{21} cm^{-2} level, even when the H I column density and stellar surface brightness maxima are spatially coincident. This is consistent with the results of other studies of dIrr systems (e.g., Hunter & Plummer 1996; Meurer et al. 1996; van Zee et al. 1997; Hunter et al. 1998). It is important to note that beam smearing may be removing the signatures of high column density gas at our current resolutions of $15''$ and $20''$, so we are cautious not to over-interpret this signature at the present time. Higher resolution and sensitivity observations of these galaxies, while requiring extensive amounts of additional observing time, would be very insightful in revealing the small-scale structure of the neutral gas disks.

3.2. Objects with Companions

The enigmatic properties of ADBS 113845+2008 led Cannon et al. (2009) to argue for an evolutionary scenario where isolation allows for a very inefficient mode of star formation or, alternatively, very inefficient gas consumption. One might naively expect that systems with similar optical properties might also be similarly isolated. We were thus somewhat surprised to discover that the majority of the sample members (five of eight systems) are in relative physical proximity to other galaxies; we hereafter refer to these systems as loose associations. H I and optical images of these loose associations are shown in Figure 11 (IC 2271), Figure 12 (KISSR 245), Figure 13 (KISSR 396), Figure 14 (KISSR 561), and Figure 15 (KISSR 572). Using the 10 kpc physical length denoted in panel (b) of each of these figures, one can discern the (projected) separation of the galaxies in each loose association. We draw attention to the (projected) separation of each association member from the compact dwarf system studied here in the caption of each figure and in Table 5; the minimum and maximum separations are 26 kpc (IC 2271 and SDSS J081808.31+243006.4) and 230 kpc (KISSR 572 and SDSS J144754.68+291929.4).

A commonly posited mechanism to initiate a burst of star formation (i.e., a starburst) is a tidal interaction. Dynamical instabilities can drive gas deep into the potential well, initiating spatially and temporally concentrated star formation (e.g., Hernquist 1989; Mihos & Hernquist 1994). While a direct signature of a tidally triggered star formation event has been difficult to produce observationally, one might suspect that extended neutral gas in the form of tidal tails might be considered to be an indirect signature of interaction-driven evolution (e.g., the extended tidal structure in the M81 group of galaxies; Yun et al. 1994).

To search for such signs of interactions amongst the loose associations studied here, we examined the moment zero (integrated H I intensity) maps and full datacubes at a variety of spatial resolutions (from 15'' to 60'') for signatures of tidal material between the compact dwarf systems and other association members. Some systems have asymmetric, low surface brightness extensions of H I gas away from the central disk (see discussion of IC 2271, KISSR 1021, KISSR 245, and KISSR 561 above) that can be interpreted as weak evidence for gravitational interactions playing a role in their recent evolution. None of the loose associations shown in Figures 11 through 15 show direct evidence of strong tidal interaction in the form of tails or diffuse gas (at the $N_{\text{HI}} \gtrsim 10^{19} \text{ cm}^{-2}$ level) connecting one system to another. The most promising candidate for a strong interaction scenario might be the loose association containing IC 2271; there is some low surface brightness H I gas surrounding multiple galaxies in this field. Given the lack of very short uv spacings in the data presented here, the surface brightness sensitivity to large-scale structure in these images is only modest. We conclude that the membership of the majority of these star-forming systems in loose

associations is intriguing but weak evidence for tidally triggered star formation events; very deep observations of these systems with the compact *VLA* D configuration could be very fruitful in further quantifying the role of interactions in initiating starburst events.

4. Comparing the Stellar and Gaseous Disks in the Compact Dwarfs Sample

The primary goal of the present investigation is to quantify the relative sizes of the neutral gas and stellar disks of each of the optically compact dwarf galaxies in our sample, thus estimating the frequency of the “giant disk” phenomenon exemplified by ADBS 113845+2008 and discussed in detail in Cannon et al. (2009). To make this comparison, we create radially averaged surface brightness profiles of each system in the optical, infrared, and H I spectral line. We measure the exponential scale lengths at optical and infrared wavelengths, and compare these to both the exponential scale length of the neutral gas disks (when possible) and to the sizes of the gaseous disks at the 10^{19} cm^{-2} level. It is important to emphasize that while this comparison does not include dynamical parameters for each system (e.g., an inclination derived from dynamical modeling of an individual galaxy’s velocity field), the comparisons discussed below do use the same corrections (when applicable) for galaxy inclination at each wavelength. Similarly, our analysis uses matched apertures between wavelengths to assure self-similar measurements.

We define a galaxy as being “resolved” in a certain image if the derived scale length or size exceeds the FWHM or beam size. Therefore, we classify systems as “resolved” in the *SDSS* r-band, the *Spitzer* 3.6 μm band, or the *Spitzer* 4.5 μm band, if the derived scale lengths exceed 1.3”, 1.66”, or 1.72”, respectively. Similarly, we classify systems as “resolved” in H I if the size of the H I disk at the 10^{19} cm^{-2} column density level exceeds the 15” beam size. We discuss the details of each of these metrics in the subsections that follow.

4.1. Optical and Infrared Surface Brightness Profiles

Optical and infrared surface brightness profiles for each of the galaxies were produced by fitting elliptical isophotes to the *SDSS* r-band, *Spitzer* 3.6 μm , and *Spitzer* 4.5 μm images using the IRAF⁷ task ELLIPSE. As noted above, some of these systems have eas-

⁷The Image Reduction and Analysis Facility (IRAF) is distributed by the National Optical Astronomy Observatory, which is operated by AURA, Inc., under cooperative agreement with the National Science Foundation.

ily identifiable foreground stars that can contaminate the surface brightness profiles [e.g., ADBS 113845+2008 (Figure 4) and KISSR 561 (Figure 8)]. Such foreground objects were masked by hand using the IRAF task FIXPIX.

For each system, the position angle and inclination were determined from the *SDSS* r-band image. When a system was extended in one dimension, the position angle was defined as that angle east of north that aligns with the larger projected optical axis. The inclination was defined by $i = \cos^{-1} \left(\frac{b}{a} \right)$ where a and b are the major and minor axes, respectively. The ellipse parameters used to derive the isophotal photometry are given in Table 6. Surface photometry was measured in elliptical isophotes incremented in one-pixel steps along the major axis (0.4'' per ellipse for the *SDSS* images and 0.6'' per ellipse for the *Spitzer* images). The r-band ellipses are shown in red in Figures 3 through 10, while the infrared ellipses are shown in green in Figures 5 through 10.

Figures 16 and 17 show the resulting surface brightness plots for all eight of the sample galaxies. As expected based on the selection criteria used to create the sample (two of which were an optical radius less than 3'' and an upper limit to the recessional velocity or distance; see discussion in § 2 above), the profiles are all centrally peaked and show little structure throughout the optical disks of the galaxies. While there is some variation in the steepness of the profile in the inner regions of the systems (i.e., within the inner few arcseconds), it is immediately obvious that each system harbors an exceptionally compact stellar component.

To quantify the sizes of these compact stellar populations, we next derived the scale lengths of each system in the *SDSS* r-band and in the *Spitzer* 3.6 μm and 4.5 μm bands. In deriving these profiles, we follow the methodology in de Blok et al. (1995). Using logarithmic units of mag arcsec^{-2} , a very good approximation for the exponential disk component of the optical radial profile can be made using:

$$\mu(r) = \mu_o + 1.086 \left(\frac{r}{h} \right) \quad (1)$$

where μ_o is the central surface brightness in units of mag arcsec^{-2} , r is the radius, $\mu(r)$ is the surface brightness in units of mag arcsec^{-2} as a function of radius, and h is the scale length. Table 7 provides the calculated scale lengths (in both angular and in physical units) at each wavelength, derived from the profiles shown in Figures 16 and 17, with upper limit errors of 25% at each ellipse location. Note that we use the nomenclature of h_r , $h_{3.6}$, and $h_{4.5}$ to denote the scale lengths (in angular units and in physical units of kpc) of each galaxy in the *SDSS* r-band, the *Spitzer* 3.6 μm band, and the *Spitzer* 4.5 μm band, respectively.

The scale lengths presented in Table 7 show that all of the galaxies are resolved in at least one optical or infrared image, and that most are resolved in both. Recall that the FWHM of the *SDSS* r-band, *Spitzer* 3.6 μm , and *Spitzer* 4.5 μm images are 1.3'', 1.66'', and

1.72", respectively. The h_r values in Table 7 show that all systems except for KISSR 245 are resolved in the *SDSS* images (that is, h_r exceeds the 1.3" FWHM of the *SDSS* r-band images). The h_r value for KISSR 245 is formally smaller than the FWHM, although it is consistent within the errorbar. Similarly, *Spitzer* resolves each galaxy; note, however, that the scale lengths of KISSR 245 at 3.6 μm and of KISSR 1021 at 4.5 μm are consistent with the FWHM, given the errorbars.

The optical and infrared scale lengths in Table 7 quantify the sizes of the compact stellar components of the sample galaxies. At the adopted distances, the stellar component of each system has an r-band scale length much less than 1 kpc. All systems have $h_r \leq 0.5$ kpc, except for KISSR 561. Moving to the infrared, the scale lengths increase. This is exactly the behavior expected of an older and non-star forming stellar population. While each of the infrared scale lengths exceeds the r-band value, it is remarkable to note that each system is still exceptionally compact even when considering the older stellar populations. For example, at 4.5 μm , some systems have scale lengths slightly larger than 1 kpc (KISSR 278, KISSR 561, KISSR 572), but others show very little increase in scale length with increasing wavelength (consider KISSR 1021, whose scale length does not change between the optical and the infrared, within the measurement errors).

4.2. H I Surface Brightness Profiles

Having quantitatively established the compact nature of the stellar population of each of the sample galaxies, we now seek to quantify the sizes of the H I neutral gas disks via two methods. First, we derive radially averaged surface brightness profiles for each system; when possible, we use these profiles to derive an exponential scale length. Second, we quantify the size of the disks at the 10^{19} cm^{-2} levels. We discuss each method in detail below.

We begin by creating radial H I surface brightness profiles for each of the galaxies using the 15" beam images and the GIPSY⁸ task ELLINT. As an inspection of Figures 3 through 10 shows, the neutral gas disks studied here are larger than the beam size for five of the eight galaxies (excluding KISSR 278, KISSR 396, and KISSR 572). A detailed dynamical analysis is only possible for ADBS 113845+2008; this precludes the derivation of kinematic position angles and inclinations for most galaxies. In order to assure an accurate comparison of stellar and gaseous properties, we thus use the same position angles and inclinations as derived using the *SDSS* r-band images (see Table 6 and the detailed discussion in § 4.1 above). These ellipses are shown in blue in Figures 3 through 10. A semi-major axis and

⁸The Groningen Image Processing System.

step size of $5''$ was used to create each of the H I profiles; technically this means that the profiles we discuss below are oversampled (compared to the $15''$ beam size) by a factor of 3. However, this oversampling does allow us to extract meaningful radially averaged surface brightness profiles.

Figures 18 and 19 show these surface brightness profiles for each of the eight sample galaxies. As was evident from the surface density images presented in § 3.1, most of the sample galaxies have H I surface brightness profiles that are centrally peaked at the resolution of these observations and that fall off with radius in a more or less smooth way. Note that low surface brightness features in some of the galaxies’ moment zero (integrated H I intensity) maps do cause departures from smooth profiles in the outer disks; for example, the low surface brightness feature extending to the southwest of KISSR 245 in Figure 5 is easily identified as the slight increase in H I surface density between $\sim 25''$ and $\sim 50''$ in Figure 18.

The obvious exception to this trend is ADBS 113845+2008, whose radially averaged H I surface density profile (created with the optically derived inclination and position angle discussed above, and shown in red in Figure 18) rises with increasing galactocentric radius, peaks, and then falls off in the outer disk. The peak surface densities are located in the broken ring structure ~ 7.5 kpc from the stellar component. A cursory comparison of the profiles in Figures 18 and 19 already reveals the striking differences between ADBS 113845+2008 and the other compact dwarf galaxies in the present sample; we discuss these differences in more detail below, and refer the interested reader to Cannon et al. (2009) for a more complete discussion of the remarkable characteristics of the ADBS 113845+2008 system.

The radial profiles shown in Figures 18 and 19 (specifically, the red profile for ADBS 113845+2008) were created using exactly the same inclinations and position angles as used to derive the optical and infrared surface brightness profiles in Figures 16 and 17. Using these neutral gas radial profiles, exponential fits were made using a version of Equation 1 converted to linear units:

$$\Sigma(r) = \Sigma_{\circ} \exp\left(-\frac{r}{h}\right) \quad (2)$$

where Σ_{\circ} is the central surface brightness of the disk in $M_{\odot} \text{ pc}^{-2}$, r is the radius, $\Sigma(r)$ is the surface brightness of the disk in $M_{\odot} \text{ pc}^{-2}$ as a function of radius, and h is the scale length (de Blok et al. 1995). We hereafter refer to the H I scale length derived using this equation as h_{HI} . We tabulate the derived h_{HI} values in Table 7. For all of the systems except ADBS 113845+2008, the calculated values of h_{HI} are smaller than the beam size. Formally, this metric to measure the size of the H I disks only provides meaningful results when it can be fit over multiple independent beams. As noted above, our radially averaged profiles required over-sampling by a factor of three. While the sizes of the H I disks based on the h_{HI} metric are interesting, and we discuss these briefly below, we seek an alternative measure of

the size of the neutral gas disks of these galaxies.

It is obvious from the neutral gas morphology (Figure 3) and surface brightness profile (Figure 18) of ADBS 113845+2008 that an exponential scale length is undefined for a disk whose morphology is not centrally concentrated. While we considered fitting the outer disk of ADBS 113845+2008 (i.e., that region at radii larger than that of the broken H I ring) with an exponential function, the striking disparity between the neutral gas and stellar disks of this system warrants caution against such an approach. Due to the remarkable qualities of this galaxy’s neutral gas disk, we thus do not calculate an exponential H I scale length. The properties of ADBS 113845+2008 naturally require a second metric for the size of the neutral gas disks of these systems.

To address these issues, we thus use the radially averaged H I surface density profiles in Figures 18 and 19 to determine the (radially averaged) size of the H I disk at the 10^{19} cm^{-2} column density level. This column density corresponds to a mass surface density of $0.08 \text{ M}_{\odot} \text{ pc}^{-2}$; recall from the discussion in § 2.2 that this emission is above the 2σ level in at least 3 consecutive channels. We extract the radii of the sample galaxies at this level (hereafter referred to as R_{HI}) from Figures 18 and 19 and tabulate the values in Table 7; note that Cannon et al. (2009) quantified the physical size of the ADBS 113845+2008 disk in the same manner. As expected, $R_{\text{HI}} > h_{\text{HI}}$ in all systems where both quantities are defined. It is important to stress that for KISSR 245, KISSR 278, KISSR 396, and KISSR 572, R_{HI} is equal (within errors) to the beam size; this means that the R_{HI} metric for these galaxies is formally an upper limit (but note that KISSR 245 does have H I gas extending to the southwest, well beyond a single beam size). These four systems are “unresolved” by the present observations (that is, $R_{\text{HI}} \lesssim \text{beam size}$, thus the R_{HI} and related values being listed as upper limits in Tables 7 and 8); they may harbor smaller neutral gas components than calculated here. We discuss the ratios of both $h_{\text{HI}}/h_{\text{r}}$ and $R_{\text{HI}}/h_{\text{r}}$ for all eight sample galaxies in § 4.3.

We again note that no kinematic constraints are used to derive the scale lengths or disk sizes discussed here; the profiles shown in Figures 16 through 19 use only optically-derived position angles and inclinations. Since seven of the eight galaxies are not sufficiently resolved to undertake a robust dynamical analysis, we can only test these dependences for the one system that does have a full kinematic model, ADBS 113845+2008. To test how using the position angles and inclinations derived from the optical images affect our calculations (as opposed to using those derived from the H I dynamics), we show three radial mass surface density profiles for ADBS 113845+2008 in Figure 18. The red profile is derived using the optical inclination (0°) and position angle (0°) and is discussed above. The blue profile uses the dynamically-derived position angle (155°) and inclination (30°) from Cannon et al. (2009). The green profile uses the same position angle (155°) as in Cannon et al. (2009),

but assumes a larger value for the galaxy’s inclination angle (60°). Since h_{HI} is undefined for ADBS 113845+2008, it is difficult to use this test to assess the dependence of H I scale length on inclination or position angle. The R_{HI} values, on the other hand, do change slightly for these different fits ($R_{\text{HI}} = 17.3 \pm 3.5$ kpc, 18.1 ± 3.6 kpc, and 22.3 ± 4.5 kpc, for the red, blue, and green profiles in Figure 18, respectively), but the resulting H I disk radii are equal within the (substantial) errorbars. While differences from one system to another are expected, this simple test gives a baseline for how to interpret the measurements made using the position angles and inclinations derived from the *SDSS* r-band images within the rest of the sample. We consider the R_{HI} values for IC 2271, ADBS 113845+2008, KISSR 561, and KISSR 1021 to be accurate representations of their (average) physical size at the 10^{19} cm^{-2} level. The R_{HI} values in Table 7 for the other four systems should be considered upper limits on the physical size of each neutral gas disk.

When available, we also tested how the disk size measurements change when using C configuration versus D configuration data. This comparison can only be made for ADBS 113845+2008 and IC 2271. The scale length measurement of IC 2271 with the lower resolution D configuration data is $h_{\text{HI}} = 2.90 \pm 0.73$ kpc ($20.0'' \pm 5.0''$); this can be compared with the $h_{\text{HI}} = 1.72 \pm 0.43$ kpc ($11.9'' \pm 3.0''$) value derived from the C configuration data only (see Table 7). The radii of the galaxy disks, when using the C versus D configuration datasets, change from $R_{\text{HI}} = 8.74 \pm 2.19$ kpc to 11.6 ± 2.9 kpc (IC 2271) and from 17.3 ± 4.3 kpc to 21.6 ± 5.4 kpc (ADBS 113845+2008). While these increases are slightly larger than the sizes of the errorbars, we conclude that there is only a modest dependency of the size estimates of these galaxy disks on the use of only the C configuration data. Given that our analysis uses the same imaging strategy for all systems, the surface brightness sensitivity of each dataset is very comparable.

4.3. On the Frequency of the “Giant Disk” Phenomenon in Compact Dwarf Galaxies

We can now compare, in a quantitative sense, the relative sizes of the stellar and gaseous disks of the eight galaxies in this sample. Table 8 contains the (dimensionless) ratios of h_{HI} and R_{HI} versus h_r , $h_{3.6}$, and $h_{4.5}$, for all galaxies with available data (recall that ADBS 113845+2008 has an undefined h_{HI} , and that no *Spitzer* imaging is available for ADBS 113845+2008 or for IC 2271). From the contents of this table, we note the following trends and behaviors.

As discussed in § 4.2 above, four of the eight systems have H I disks that exceed the sizes of the stellar bodies based on the R_{HI} metric (and are thus considered “resolved” in

H I). Hence, the dimensionless ratios in Table 8 for KISSR 245, KISSR 278, KISSR 396, and KISSR 572 should be considered upper limits; the actual size ratios of neutral to stellar disks may in fact be smaller for these systems. For the entire sample, the ratios of h_{HI} to r-band or infrared scale lengths (spanning a range of ~ 2 to ~ 7) are systematically smaller than the ratios of R_{HI} to the same r-band or infrared values (which span a range of ~ 4 to ~ 58). Similarly, for each individual galaxy, the relative size ratios measured using either R_{HI} or h_{HI} decrease with increasing wavelength used to measure the stellar disk size. These general trends hold across the entire sample, regardless of which tracer is used to measure the size of either the stellar or the gaseous disk.

The R_{HI}/h_r ratio for ADBS 113845+2008 (58 ± 21) is more than a factor of two larger than the same ratio for any of the other systems; if the ratios in Table 7 for the other sample members are smaller, then this reinforces the enormity of the H I disk of ADBS 113845+2008. Using the other seven sample galaxies as benchmarks, it is physically intuitive that the infrared scale length of ADBS 113845+2008 would be larger than the measured h_r value. However, the enormous R_{HI}/h_r ratio of this system, and the relative size of the broken H I ring (~ 7.5 kpc in radius) versus the optical scale length (0.30 ± 0.08 kpc), are challenging parameters to explain unless the optical body is only a high surface brightness knot in an otherwise extremely low surface brightness underlying stellar disk. We again refer the interested reader to Cannon et al. (2009) for more detailed discussion; for the purposes of this work, we interpret the remarkable properties of ADBS 113845+2008 as the signature of a “giant” H I disk.

The present sample of compact dwarf galaxies was created using consistent selection criteria; the observations and analysis have produced a uniform set of results. While the sample is small, it appears that the frequency of “giant disk” dwarf galaxies such as ADBS 113845+2008 is low. A few other examples of such systems have been identified (e.g., DDO 154, Carignan & Beaulieu 1989, Carignan & Purton 1998; NGC 2915, Meurer et al. 1996; UGC 5288, van Zee 2004; NGC 3741, Bremnes et al. 2000, Begum et al. 2005). This small collection of galaxies suggests that systems with qualities similar to ADBS 113845+2008 are comparatively rare in the local volume. A larger sample of H I observations of local compact dwarf systems could be fruitful in improving the statistics of the trends identified in Table 8.

5. Conclusions

We have presented *VLA* C configuration imaging of eight optically compact dwarf galaxies. These sources were selected to share the following common characteristics: 1) compact

stellar populations; 2) faint blue absolute magnitudes (i.e., low masses); 3) emission lines indicative of recent star formation; and 4) proximity for spatially resolved work. The sample includes the “giant disk” dwarf galaxy ADBS 113845+2008 studied in Cannon et al. (2009). The *VLA* data are supplemented by archival optical (*SDSS* r-band) and infrared (*Spitzer* 3.6 μm and 4.5 μm) imaging. We use this data suite to quantitatively address the relative sizes of the stellar and gaseous components of these galaxies.

A comparison of the morphology of the stellar and gaseous disks of each galaxy in the sample reveals that all eight systems have extremely compact (though in almost all cases resolved) stellar components; this is of course expected given the selection criteria. Seven of the eight systems in the sample harbor centrally concentrated neutral gas distributions. ADBS 113845+2008 differs from the other systems in that its neutral gas disk is structured in a broken ring that is well outside of the stellar component. In most of the other cases, the stellar and gaseous disks have surface brightness maxima that are in close physical proximity to one another.

Five of the eight systems are located in loose associations, with neighboring systems with projected separations of less than a few hundred kpc and with recessional velocities within a few hundred km s^{-1} . Some of the loose association galaxies have low surface brightness neutral gas in the outer disks that might be construed as evidence of tidal interactions. However, given the lack of very short *uv* spacings in our data, we conservatively conclude that the membership of these star-forming dwarfs in such loose associations is only weak evidence for a tidal burst trigger.

While each of the eight sample galaxies is detected in H I at meaningful significance, these *VLA* data do not allow a robust dynamical analysis in any of the systems except for ADBS 113845+2008. Thus, we concentrate on the morphological properties of the galaxies. We use the optical, infrared, and H I data to derive radially averaged surface brightness profiles that can be used to measure the sizes of both the stellar and the gaseous components. We quantify the sizes of the H I disks via both an exponential scale length (available for all systems except for ADBS 113845+2008) and a (radially averaged) limit of the gaseous disk at the 10^{19} cm^{-2} column density ($0.08 \text{ M}_{\odot} \text{ pc}^{-2}$) level.

We find that four of the eight systems (specifically, IC 2271, ADBS 113845+2008, KISSR 561, and KISSR 1021) have larger gaseous disks than stellar disks; the remaining four (KISSR 245, KISSR 278, KISSR 396, and KISSR 572) have only upper limits on the physical size of their H I disks (but note that KISSR 245 has low-surface brightness H I gas extending well beyond a single beam size; see Figure 5). When parameterized by an H I disk scale length, the neutral gas disks of the seven available galaxies (excluding ADBS 113845+2008) are larger than the stellar disks by factors of ~ 2 –7. When parameterized by the size of the H I disk at the

10^{19} cm^{-2} column density level, the neutral gas disks of the eight sample galaxies (including ADBS 113845+2008) are larger than the stellar disks by factors of ~ 4 –58. For each galaxy, the relative size ratios measured using either R_{HI} or h_{HI} decrease with increasing wavelength used to measure the stellar disk size (i.e., the optical scale lengths are slightly shorter than the infrared scale lengths). If the values of R_{HI} and h_{HI} are upper limits, then these ratios decrease.

ADBS 113845+2008 stands out among the members of this sample as harboring a “giant” H I disk. While the H I-to-optical size ratios of some other members of the sample are substantial (e.g., IC 2271, KISSR 245; see Table 8), this ratio for ADBS 113845+2008 is more than twice as large as any other measured here. As discussed in Cannon et al. (2009), the physical properties of this galaxy are extreme and enigmatic; ADBS 113845+2008 has one of the largest known H I-to-optical size ratios in the local universe. Given that the present sample was selected *only* based on optically-derived properties, and that the observations of the present sample were acquired and analyzed in a uniform way, suggests that this “giant disk” dwarf galaxy is rare in the local volume. The present sample is small and is limited in number by available (single dish H I) data; the statistics behind the present results could be significantly strengthened by a larger study of additional extremely compact, star-forming dwarf galaxies in the local volume.

This research was supported by a Cottrell College Science Award from Research Corporation. JLR acknowledges support from NSF AST-000167932. The authors thank the National Radio Astronomy Observatory and Macalester College for partial support of this work, and Dr. Gustaaf van Moorsel for helpful discussions. This work is based in part on archival data obtained with the *Spitzer Space Telescope*, which is operated by the Jet Propulsion Laboratory, California Institute of Technology under a contract with NASA. Support for this work was provided by an award issued by JPL/Caltech. This work has made use of data from the *Sloan Digital Sky Survey*. Funding for the *SDSS* and *SDSS-II* has been provided by the Alfred P. Sloan Foundation, the Participating Institutions, the National Science Foundation, the U.S. Department of Energy, the National Aeronautics and Space Administration, the Japanese Monbukagakusho, the Max Planck Society, and the Higher Education Funding Council for England. The *SDSS* Web Site is <http://www.sdss.org/>. The *SDSS* is managed by the Astrophysical Research Consortium for the Participating Institutions. The Participating Institutions are the American Museum of Natural History, Astrophysical Institute Potsdam, University of Basel, University of Cambridge, Case Western Reserve University, University of Chicago, Drexel University, Fermilab, the Institute for Advanced Study, the Japan Participation Group, Johns Hopkins University, the Joint Institute for Nuclear Astrophysics, the Kavli Institute for Particle Astrophysics and Cosmology, the Korean Scientist Group,

the Chinese Academy of Sciences (LAMOST), Los Alamos National Laboratory, the Max-Planck-Institute for Astronomy (MPIA), the Max-Planck-Institute for Astrophysics (MPA), New Mexico State University, Ohio State University, University of Pittsburgh, University of Portsmouth, Princeton University, the United States Naval Observatory, and the University of Washington. This research has made use of the NASA/IPAC Extragalactic Database (NED) which is operated by the Jet Propulsion Laboratory, California Institute of Technology, under contract with the National Aeronautics and Space Administration, and NASA's Astrophysics Data System.

REFERENCES

- Aihara, H., et al. 2011, *ApJ*, 193, 29
- Begum, A., Chengalur, J. N., & Karachentsev, I. D. 2005, *A&A*, 433, L1
- Bremnes, T., Binggeli, B., & Prugniel, P. 2000, *A&AS*, 141, 211
- Briggs, D. 1995, Ph.D. thesis, New Mexico Inst. Mining and Technol.
- Brown, T. M., Heap, S. R., Hubeny, I., Lanz, T., & Lindler, D. 2002, *ApJ*, 579, L75
- Bureau, M., Freeman, K. C., Pfitzner, D. W., & Meurer, G. R. 1999, *AJ*, 118, 2158
- Cannon, J. M., Salzer, J. J., & Rosenberg, J. L. 2009, *ApJ*, 696, 2104
- Carignan, C., & Beaulieu, S. 1989, *ApJ*, 347, 760
- Carignan, C., & Purton, C. 1998, *ApJ*, 506, 125
- Clark, B. G. 1980, *A&A*, 89, 377
- Cornwell, T. J. 2008, *arXiv:0806.2228v1*
- de Blok, W. J. G., van der Hulst, J. M., & Bothun, G. D. 1995, *MNRAS*, 274, 235
- Ekta, Chengalur, J. N., & Pustilnik, S. A. 2006, *MNRAS*, 372, 853
- Elson, E. C., de Blok, W. J. G., & Kraan-Korteweg, R. C. 2010, *MNRAS*, 404, 2061
- Hernquist, L. 1989, *Nature*, 340, 687
- Högbom, J. A. 1974, *A&AS*, 15, 417
- Hunter, D. A., & Plummer, J. D. 1996, *ApJ*, 462, 732
- Hunter, D. A., Elmegreen, B. G., & Baker, A. L. 1998, *ApJ*, 493, 595
- Kennicutt, R. C., Jr. 1989, *ApJ*, 344, 685
- Kennicutt, R. C., Jr. 1998, *ApJ*, 498, 541
- Lee, J. C., Salzer, J. J., Impey, C., Thuan, T. X., & Gronwall, C. 2002, *AJ*, 124, 3088
- Martínez-Delgado, D., Romanowsky, A. J., Gabany, R. J., et al. 2012, *ApJ*, 748, L24
- Meurer, G. R., Mackie, G., & Carignan, C., 1994, *AJ*, 107, 2021

- Meurer, G. R., Carignan, C., Beaulieu, S. F., & Freeman, K. C. 1996, *AJ*, 111, 1551
- Mihos, J. C., & Hernquist, L. 1994, *ApJ*, 425, L13
- Miyauchi-Isobe, N. & Maehara, H. 2000, *PNAOJ*, 6, 1
- Östlin, G., Amram, P., Bergvall, N., et al. 2001, *A&A*, 374, 800
- Pisano, D. J., Wilcots, E. M., & Liu, C. T., 2002, *ApJ*, 142, 161
- Rosenberg, J. L., & Schneider, S. E., 2000, *ApJ*, 130, 177
- Rosenberg, J. L., & Schneider, S. E. 2002, *ApJ*, 567, 247
- Salzer, J. J., et al. 2000, *AJ*, 120, 80
- Salzer, J. J., et al. 2001, *AJ*, 121, 66
- Salzer, J. J., et al. 2002, *AJ*, 123, 1292
- Simpson, C. E., Hunter, D. A., Nordgren, T. E., et al. 2011, *AJ*, 142, 82
- Skillman, E. D. 1987, *Star Formation in Galaxies* (NASA Conf. Publ. 2466), ed. C. J. Lonsdale Persson (Washington, DC: NASA), 263
- Thuan, T. X., & Martin, G. E. 1981, *ApJ*, 247, 823
- Thuan, T. X. 1983, *ApJ*, 268, 667
- Thuan, T. X., Hibbard, J. E., & Lévrier, F. 2004, *AJ*, 128, 617
- Walter, F., Brinks, E., Duric, N., & Klein, U. 1997, *AJ*, 113, 2031
- van Zee, L., Haynes, M. P., Salzer, J. J., & Broeils, A. H. 1997, *AJ*, 113, 1618
- van Zee, L., Skillman, E. D., & Salzer, J. J. 1998, *AJ*, 116, 1186
- van Zee, L. 2004, *Bulletin of the American Astronomical Society*, 36, 1495
- van Zee, L., Cannon, J. M., & Skillman, E. D. 2006, *Bulletin of the American Astronomical Society*, 38, #167.06
- Yun, M. S., Ho, P. T. P., & Lo, K. Y. 1994, *Nature*, 372, 530

Table 1. Basic Parameters of Sample Galaxies

Galaxy Name	R.A. (J2000)	DEC (J2000)	$V_{\text{sys}}^{\text{a}}$ (km s^{-1})	Distance ^b (Mpc)	H I Mass ($10^7 M_{\odot}$)	Single Dish H I Mass ($10^7 M_{\odot}$)
IC 2271	08:18:19.7	24:31:37	2184 ± 10	29.9	25.1 ± 6.3	$101^{\text{c,d}}$
ADBS 113845+2008	11:38:45.2	20:08:24	3054 ± 3	41.8	40.2 ± 10.1	84.6^{c}
KISSR 245	13:16:27.9	29:25:11	4762 ± 5	65.2	13.0 ± 3.3	28.4^{e}
KISSR 278	13:23:37.7	29:17:17	4022 ± 5	55.1	4.4 ± 1.1	12.0^{e}
KISSR 396	13:57:10.0	29:13:10	2238 ± 5	30.7	1.0 ± 0.3	11.6^{e}
KISSR 561	14:29:53.6	29:20:11	3750 ± 5	51.4	34.3 ± 8.6	56.5^{e}
KISSR 572	14:46:48.2	29:25:18	3693 ± 5	50.6	2.3 ± 0.6	16.6^{e}
KISSR 1021	16:19:02.5	29:10:22	2519 ± 5	34.5	7.0 ± 1.8	14.5^{e}

^aDerived from H I global profiles using the full width at half maximum.

^bAssumes $H_0 = 73 \text{ km s}^{-1} \text{ Mpc}^{-1}$.

^cCalculated from the work of Rosenberg & Schneider (2000).

^dRosenberg & Schneider (2000) quote an *Arecibo* drift scan detection of IC 2271 in the *ADBS*. Since single drift scan observations do not assure that a source passes through the center of the beam, the resulting flux integral is uncertain. Thus, the value quoted for IC 2271 is from subsequent *VLA* D configuration snapshot observations.

^eCalculated from the work of Lee et al. (2002).

Table 2. *VLA* Observation Information

Galaxy Name	Date of Observation	Total Time on Source (Minutes)	Total Bandwidth (MHz)	Number of Channels	Channel Separation (km s^{-1})
IC 2271	2006 Oct. 31	241	3.12	64	10.30
ADBS 113845+2008	2006 Oct. 31	245	1.56	128	2.58
KISSR 245	2008 Apr. 23	252	3.12	128	5.15
KISSR 278	2008 Apr. 29	253	3.12	128	5.15
KISSR 396	2008 May 1	254	3.12	128	5.15
KISSR 561	2008 May 13	252	3.12	128	5.15
KISSR 572	2008 May 8	251	3.12	128	5.15
KISSR 1021	2008 May 15	255	3.12	128	5.15

Table 3. *VLA* Observations of the Compact Dwarfs Sample

Galaxy Name	Velocity Range (km s^{-1})	RMS noise (mJy Bm^{-1})	S_{HI} (<i>VLA</i>) (Jy km s^{-1})	S_{HI} (Single Dish) (Jy km s^{-1})
IC 2271	2121 - 2246	0.39	1.22 ± 0.12	$4.702^{\text{a},\text{b}}$
ADBS 113845+2008	2987 - 3117	0.73	0.98 ± 0.10	1.982^{a}
KISSR 245	4744 - 4779	0.52	0.13 ± 0.01	0.28^{c}
KISSR 278	4014 - 4030	0.48	0.062 ± 0.006	0.17^{c}
KISSR 396	2221 - 2253	0.53	0.043 ± 0.004	0.51^{c}
KISSR 561	3695 - 3809	0.50	0.55 ± 0.06	0.89^{c}
KISSR 572	3688 - 3699	0.48	0.038 ± 0.004	0.27^{c}
KISSR 1021	2473 - 2562	0.46	0.25 ± 0.03	0.51^{c}

^aRosenberg & Schneider (2000)

^bRosenberg & Schneider (2000) quote an *Arecibo* drift scan detection of IC 2271 in the *ADBS*. Since single drift scan observations do not assure that a source passes through the center of the beam, the resulting flux integral is uncertain. Thus, the value quoted for IC 2271 is from subsequent *VLA* D configuration snapshot observations.

^cLee et al. (2002)

Table 4. UVTAPER Tests

Galaxy Name	S_{HI} (Jy km s ⁻¹)		
	15'' ^a	30'' ^a	60'' ^a
IC 2271	1.2	1.5	1.5
ADBS 113845+2008	0.98	0.90	0.90
KISSR 245	0.13	0.14	0.15
KISSR 278	0.062	0.30	- ^b
KISSR 396	0.043	0.038	0.039
KISSR 561	0.55	0.65	0.66
KISSR 572	0.038	0.028	- ^b
KISSR 1021	0.25	0.35	0.23

^aCircular beamsize created from changing the parameter UVTAPER in the AIPS task IMAGR.

^bGalaxy could not be found in three or more consecutive channels when blanking through the cube.

Table 5. Relative Distances Between Companion Galaxies

Target Galaxy	Companion Galaxy(s)	Positional Offset (arcsec)	Velocity Offset (km s ⁻¹)	Minimum Separation (kpc)
IC 2271	ADBS J081707+2433	995	121	144
	IC 2267	790	146	115
	SDSS J081808.31+243006.4	180	105	26
KISSR 245	MAPS-NGP_O_323_0594797	477	12	151
KISSR 396	NGC 5375	270	137	40
	NGC 5375A	633	18	94
KISSR 561	NGC 5657	861	110	215
KISSR 572	SDSS J144754.68+291929.4	936	33	230

Table 6. Ellipse Parameters for Isophotal Photometry

Galaxy Name	P.A. E of N	Inclination
IC 2271	143°	45°
ADBS 113845+2008	0°	0°
KISSR 245	0°	0°
KISSR 278	40°	73°
KISSR 396	175°	43°
KISSR 561	0°	57°
KISSR 572	60°	70°
KISSR 1021	130°	48°

Table 7. Scale Length Calculations

Galaxy Name	h_r (kpc)	$h_{3.6}$ (kpc)	$h_{4.5}$ (kpc)	h_{HI} (kpc)	R_{HI} (kpc)
IC 2271	0.33 ± 0.08	N/A	N/A	1.72 ± 0.43	8.74 ± 2.19
ADBS 113845+2008	0.30 ± 0.08	N/A	N/A	^a	17.3 ± 4.3
KISSR 245	0.38 ± 0.10	0.55 ± 0.14	0.70 ± 0.18	2.48 ± 0.62	$<8.28 \pm 2.07$
KISSR 278	0.41 ± 0.10	0.80 ± 0.20	1.36 ± 0.34	2.64 ± 0.66	$<6.19 \pm 1.55$
KISSR 396	0.19 ± 0.05	0.31 ± 0.08	0.36 ± 0.09	0.78 ± 0.20	$<2.65 \pm 0.66$
KISSR 561	0.72 ± 0.18	1.30 ± 0.33	1.20 ± 0.30	2.59 ± 0.65	11.8 ± 3.0
KISSR 572	0.50 ± 0.13	0.77 ± 0.19	1.18 ± 0.30	2.19 ± 0.55	$<4.64 \pm 1.16$
KISSR 1021	0.29 ± 0.07	0.37 ± 0.09	0.31 ± 0.08	1.18 ± 0.30	5.39 ± 1.35
Galaxy Name	h_r (arcsec)	$h_{3.6}$ (arcsec)	$h_{4.5}$ (arcsec)	h_{HI} (arcsec)	R_{HI} (arcsec)
IC 2271	2.29 ± 0.57	N/A	N/A	11.9 ± 3.0	60.3 ± 15.1
ADBS 113845+2008	1.44 ± 0.36	N/A	N/A	^a	85.3 ± 21.3
KISSR 245	1.18 ± 0.30	1.71 ± 0.43	2.21 ± 0.55	7.84 ± 1.96	$<26.2 \pm 6.6$
KISSR 278	1.51 ± 0.38	2.99 ± 0.75	5.12 ± 1.28	9.88 ± 2.47	$<23.2 \pm 5.8$
KISSR 396	1.33 ± 0.33	2.13 ± 0.53	2.50 ± 0.63	5.25 ± 1.31	$<17.8 \pm 4.5$
KISSR 561	2.93 ± 0.73	5.27 ± 1.32	4.86 ± 1.22	10.4 ± 2.6	47.4 ± 11.9
KISSR 572	2.07 ± 0.52	3.18 ± 0.80	4.87 ± 1.22	8.93 ± 2.23	$<18.9 \pm 4.7$
KISSR 1021	1.74 ± 0.44	2.23 ± 0.56	1.86 ± 0.47	7.05 ± 1.76	32.2 ± 8.1

^aThe value of h_{HI} for ADBS 113845+2008 cannot be accurately determined due to the H I central depression and outer high column density ring.

Table 8. Relative Sizes of the Stellar and Gaseous Disks

Galaxy	$h_{\text{HI}}/h_{\text{r}}$	$R_{\text{HI}}/h_{\text{r}}$	$h_{\text{HI}}/h_{3.6}$	$R_{\text{HI}}/h_{3.6}$	$h_{\text{HI}}/h_{4.5}$	$R_{\text{HI}}/h_{4.5}$
IC 2271	5.2 ± 1.8	26 ± 9	N/A	N/A	N/A	N/A
ADBS 113845+2008	- ^a	58 ± 21	N/A	N/A	N/A	N/A
KISSR 245	6.5 ± 2.4	$<22 \pm 8$	4.5 ± 1.6	$<15 \pm 5$	3.5 ± 1.3	$<12 \pm 4.2$
KISSR 278	6.4 ± 2.2	$<15 \pm 5$	3.3 ± 1.2	$<7.7 \pm 2.7$	1.9 ± 0.7	$<4.6 \pm 1.6$
KISSR 396	4.1 ± 1.5	$<14 \pm 5$	2.5 ± 0.9	$<8.5 \pm 3.0$	2.2 ± 0.8	$<7.4 \pm 2.6$
KISSR 561	3.6 ± 1.3	16 ± 6	2.0 ± 0.7	9.1 ± 3.2	2.2 ± 0.8	9.8 ± 3.5
KISSR 572	4.4 ± 1.6	$<9.3 \pm 3.3$	2.8 ± 1.0	$<6.0 \pm 2.1$	1.9 ± 0.7	$<3.9 \pm 1.4$
KISSR 1021	4.1 ± 1.4	19 ± 6	3.2 ± 1.1	14.6 ± 5.2	3.8 ± 1.4	17 ± 6.2

^aThe value of h_{HI} for ADBS 113845+2008 cannot be accurately determined due to the H I central depression and outer high column density ring.

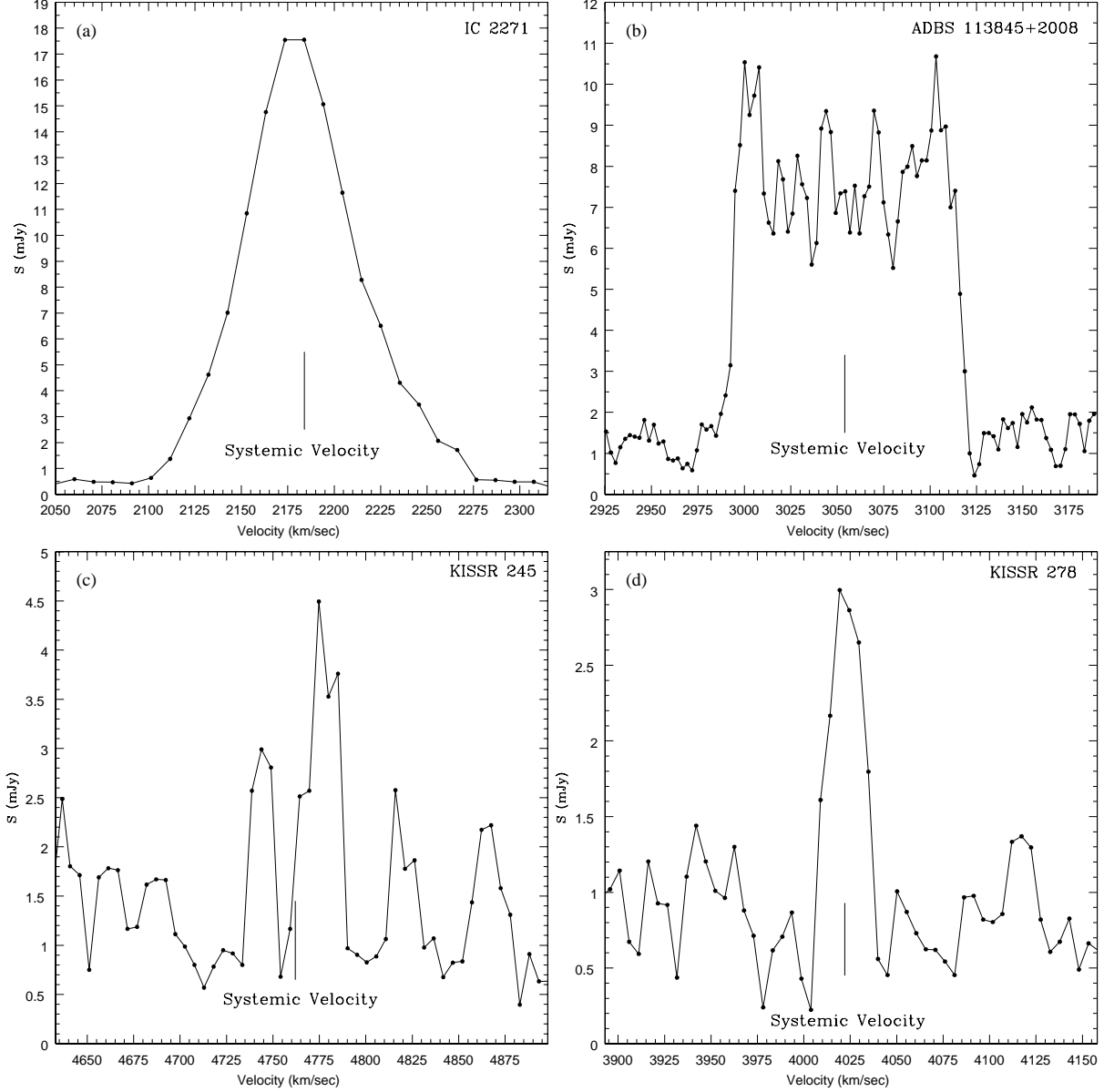


Fig. 1.— Global H I profiles for IC 2271 (a), ADBS 113845+2008 (b), KISSR 245 (c), and KISSR 278 (d), with the derived systemic velocities shown. These profiles were produced by determining the flux in each channel after the by-hand blanking process discussed in § 2.2. The flux in each channel was boxcar averaged with the flux from the two adjacent channels to create the profiles shown here.

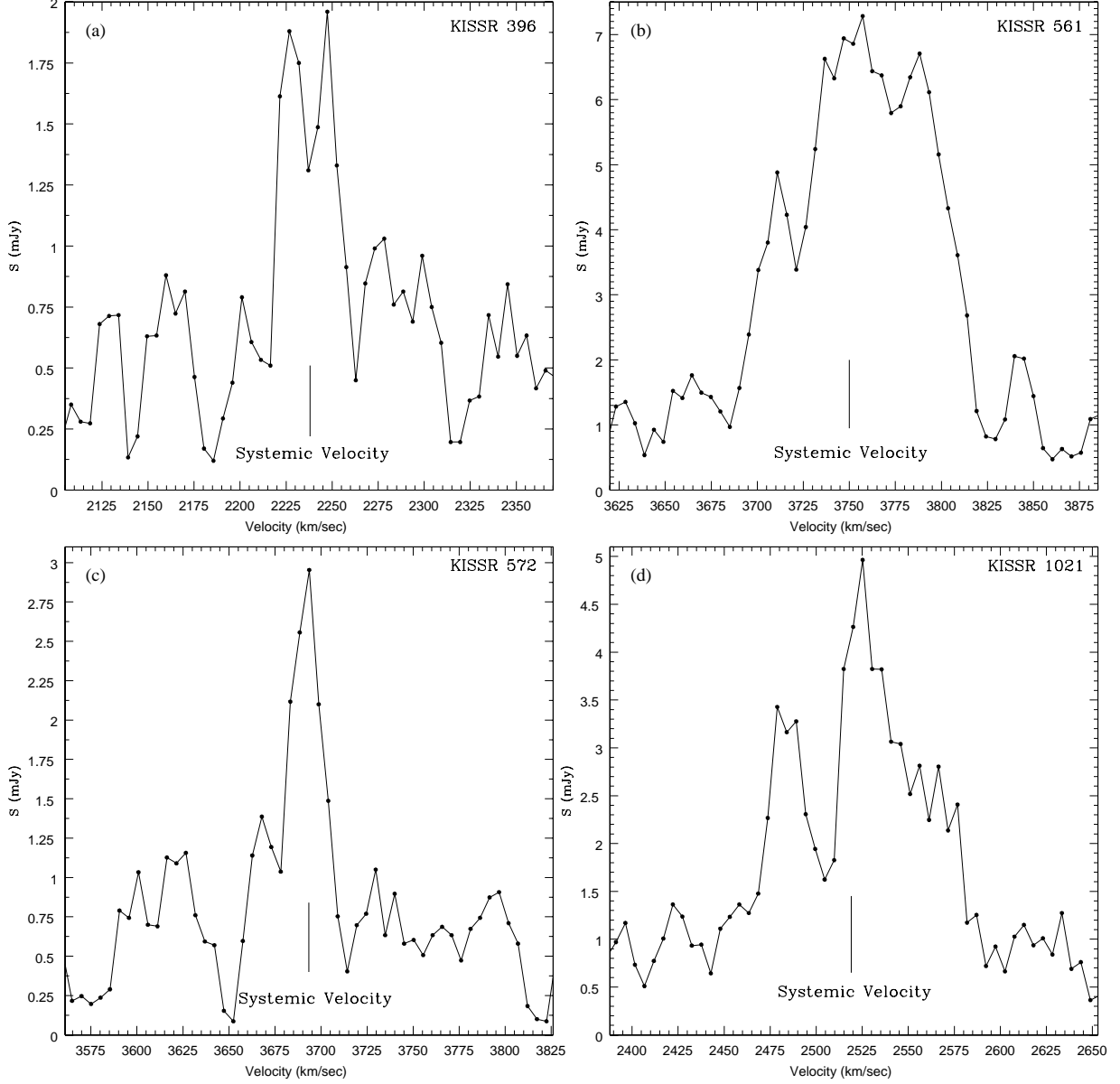


Fig. 2.— Same as Figure 1, for KISSR 396 (a), KISSR 561 (b), KISSR 572 (c), and KISSR 1021 (d).

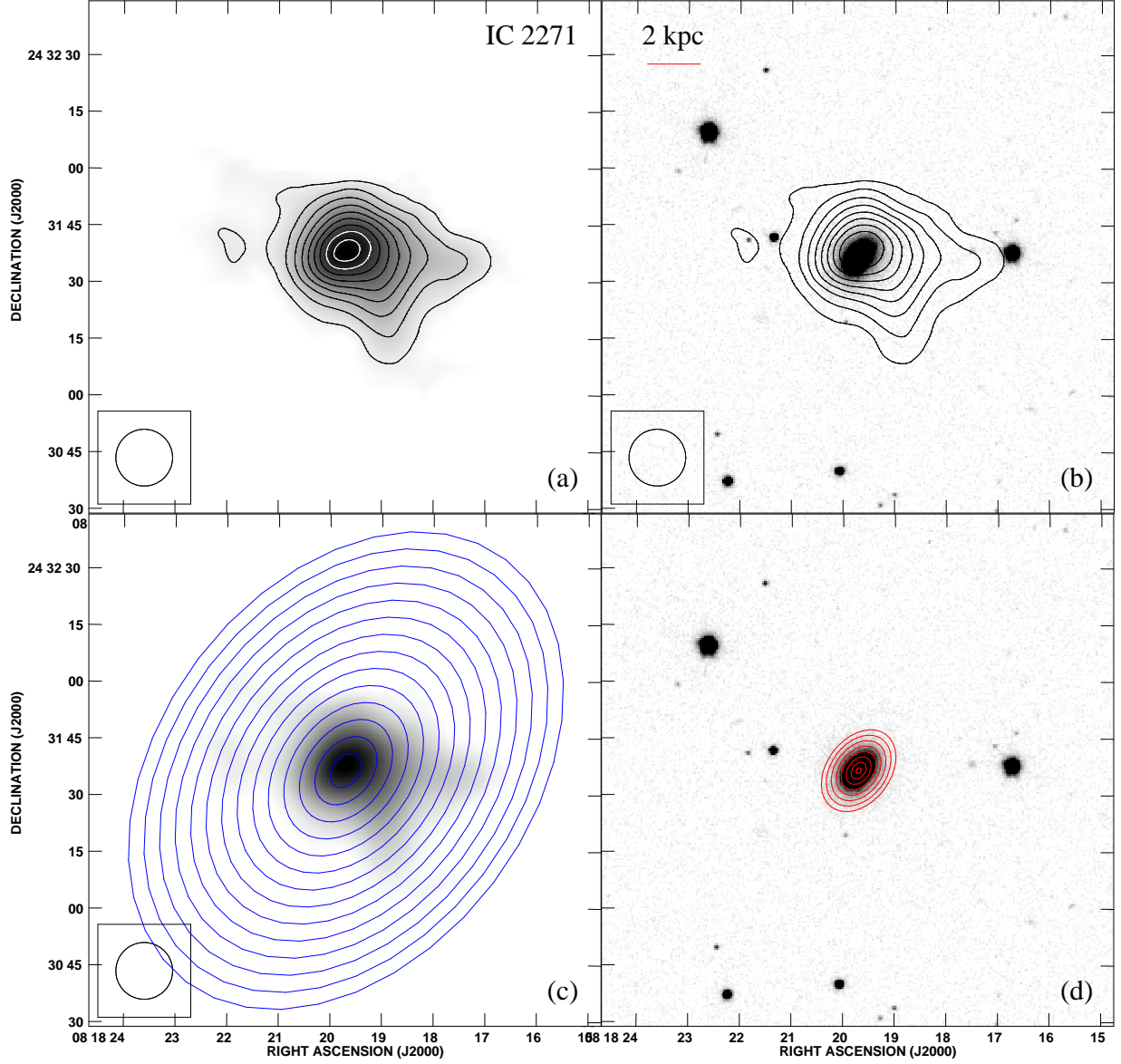


Fig. 3.— VLA and SDSS images of IC 2271. Panels (a) and (c) show the H I column density image at 15'' resolution. Panels (b) and (d) show the SDSS r-band image. The H I column density contours in panels (a) and (b) are at the (2, 4, 6, 8, 10, 12, 14, 16, 18) $\times 10^{20} \text{ cm}^{-2}$ levels. The ellipses are those used to determine the H I (c; see § 4.2) and optical (d; see § 4.1) radial profiles. The ellipses in panel (d) are shown as every fourth to be visible at this size. The red bar in panel (b) denotes a physical length of 2 kpc at the adopted distance.

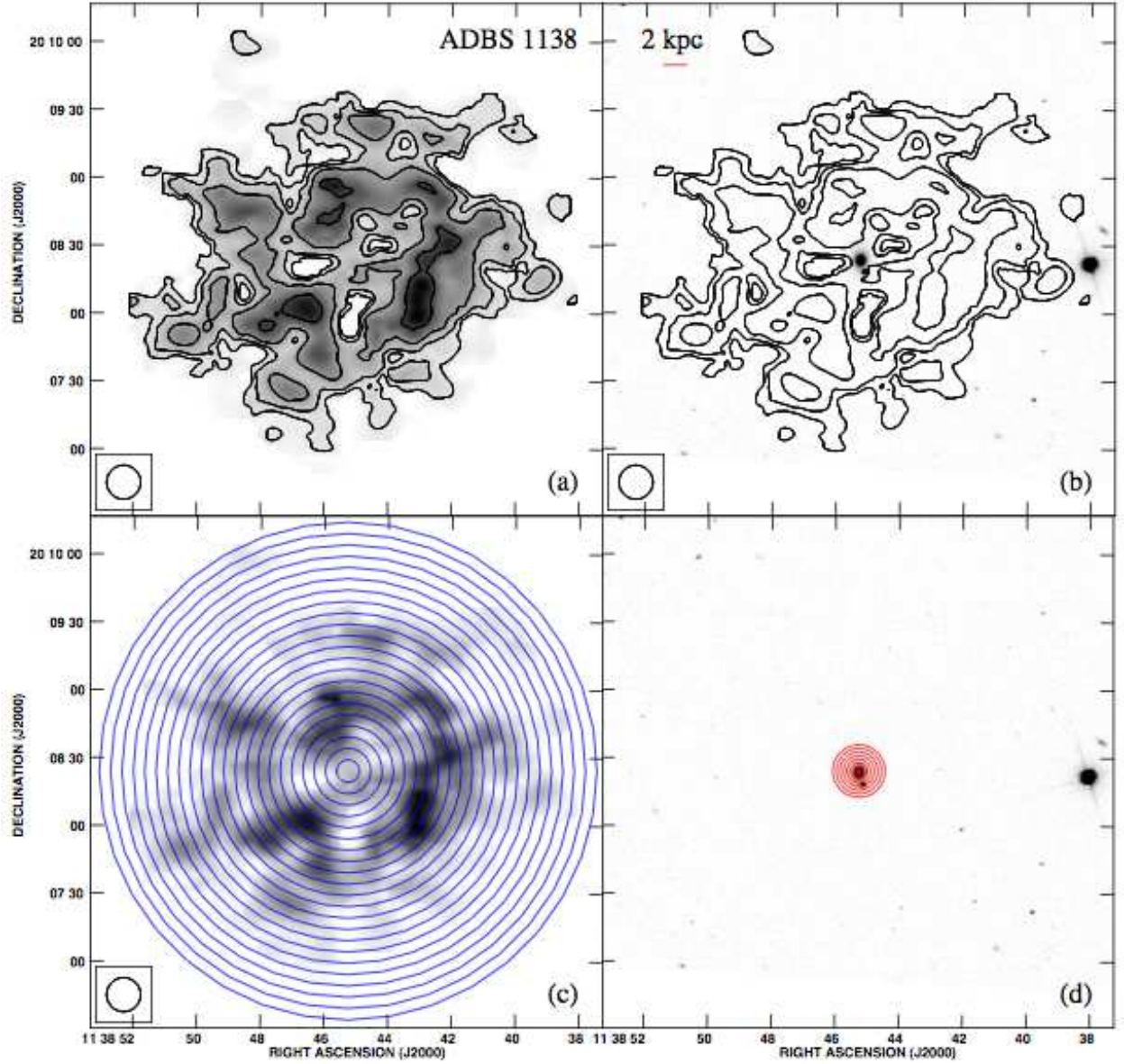


Fig. 4.— *VLA* and *SDSS* images of ADBS 113845+2008. Panels (a) and (c) show the H I column density image at 15'' resolution. Panels (b) and (d) show the *SDSS* r-band image. The H I column density contours in panels (a) and (b) are at the $(0.2, 0.4, 0.8, 1.6) \times 10^{20} \text{ cm}^{-2}$ levels. The ellipses are those used to determine the H I (c; see § 4.2) and optical (d; see § 4.1) radial profiles. The ellipses in panel (d) are shown as every fourth to be visible at this size. Note the extremely optically compact nature of ADBS 113845+2008, especially when compared to the foreground star immediately to the southwest of the galaxy. The red bar in panel (b) denotes a physical length of 2 kpc at the adopted distance.

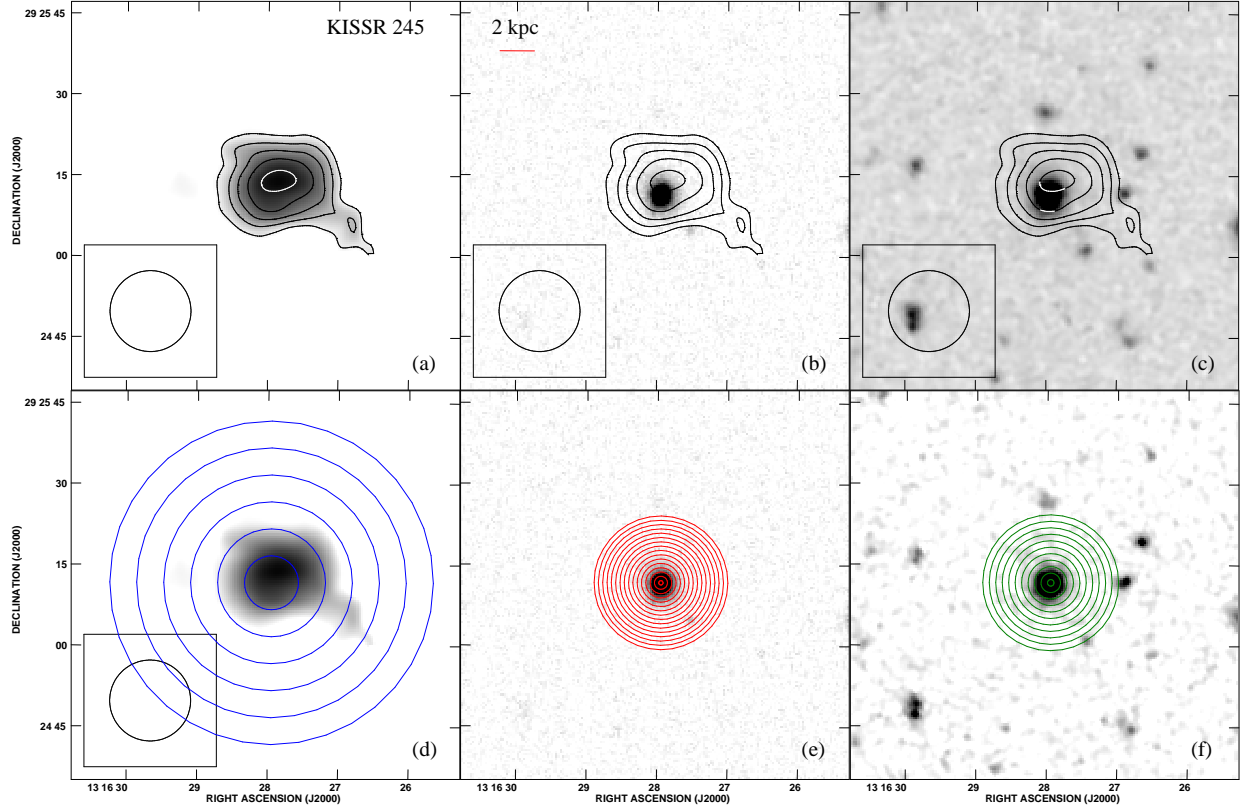


Fig. 5.— *VLA*, *SDSS*, and *Spitzer* images of KISSR 245. Panels (a) and (d) show the H I column density at $15''$ resolution; panels (b) and (e) show the *SDSS* r-band image; panels (c) and (f) show the *Spitzer* 3.6 μm (c) and 4.5 μm (f) images. The contours in panels (a) through (c) are at the $(0.8, 1, 1.2, 1.4, 1.6) \times 10^{20} \text{ cm}^{-2}$ levels. Panel (d) is overlaid with the isophotal ellipses used to create the H I radial profile (see § 4.2), while panels (e) and (f) are overlaid with the isophotal ellipses used to create the optical and infrared radial profiles (see § 4.1). The ellipses in panels (e) and (f) are shown as every other to be visible at this size. The red bar in panel (b) denotes a physical length of 2 kpc at the adopted distance.

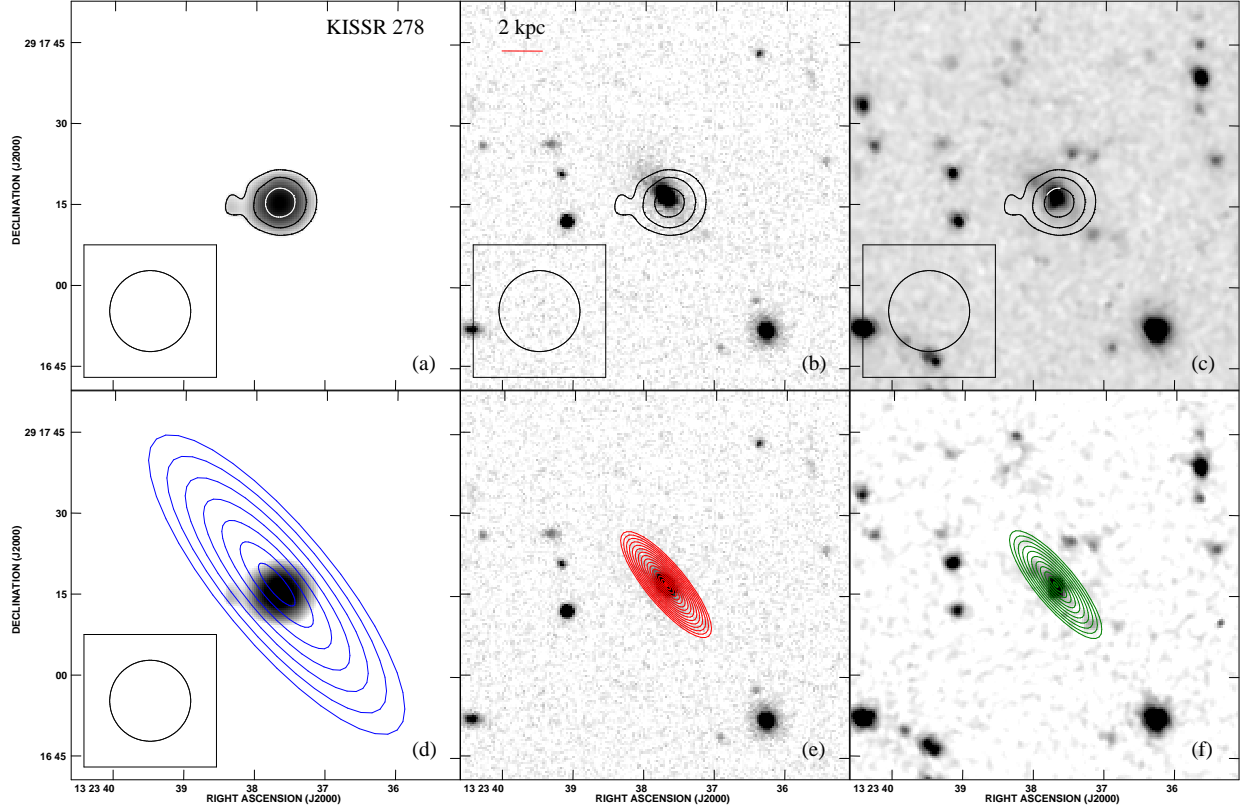


Fig. 6.— *VLA*, *SDSS* and *Spitzer* images of KISSR 278. Panels (a) and (d) show the H I column density at $15''$ resolution; panels (b) and (e) show the *SDSS* r-band image; panels (c) and (f) show the *Spitzer* $3.6\ \mu\text{m}$ (c) and $4.5\ \mu\text{m}$ (f) images. The contours in panels (a) through (c) are at the $(0.8, 1, 1.2) \times 10^{20}\ \text{cm}^{-2}$ levels. Panel (d) is overlaid with the isophotal ellipses used to create the H I radial profile (see § 4.2), while panels (e) and (f) are overlaid with the isophotal ellipses used to create the optical and infrared radial profiles (see § 4.1). The ellipses in panels (e) and (f) are shown as every other to be visible at this size. The red bar in panel (b) denotes a physical length of 2 kpc at the adopted distance.

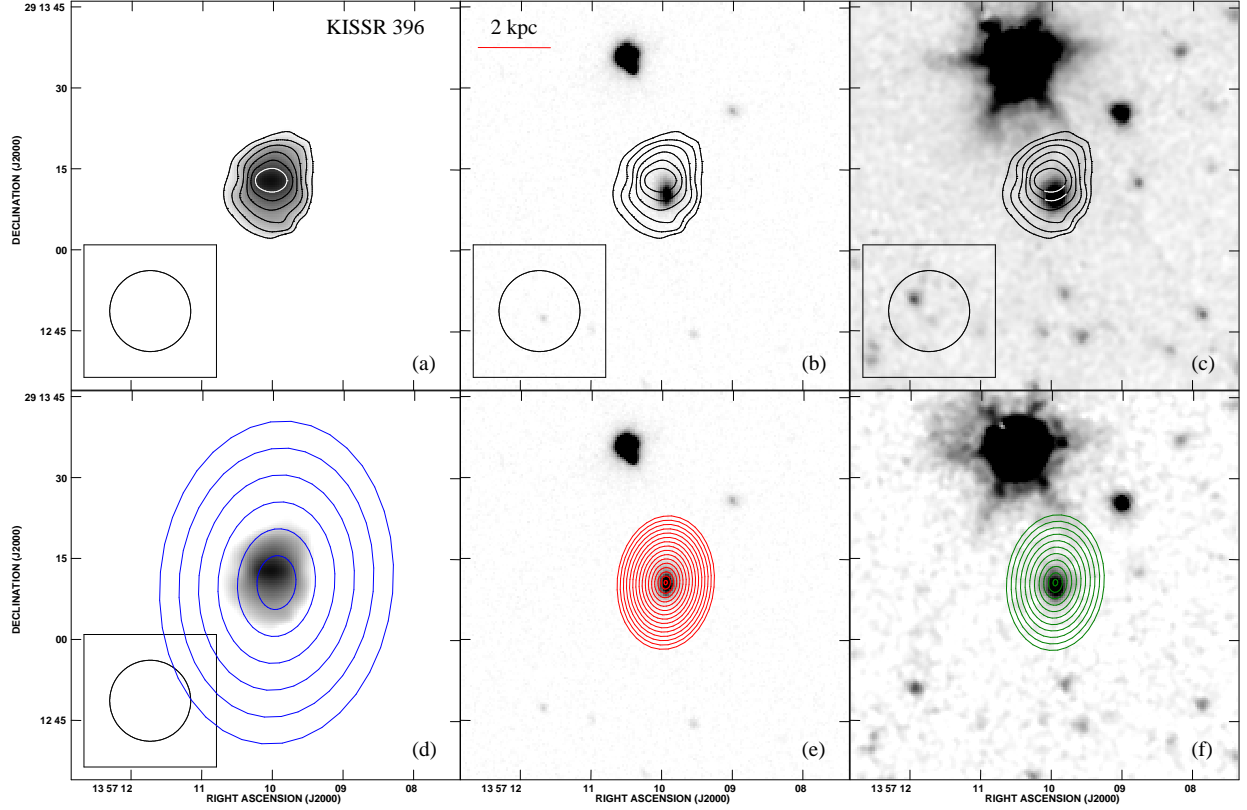


Fig. 7.— *VLA*, *SDSS* and *Spitzer* images of KISSR 396. Panels (a) and (d) show the H I column density at $15''$ resolution; panels (b) and (e) show the *SDSS* r-band image; panels (c) and (f) show the *Spitzer* $3.6 \mu\text{m}$ (c) and $4.5 \mu\text{m}$ (f) images. The contours in panels (a) through (c) are at the $(0.8, 1, 1.2, 1.4, 1.6, 1.8) \times 10^{20} \text{ cm}^{-2}$ levels. Panel (d) is overlaid with the isophotal ellipses used to create the H I radial profile (see § 4.2), while panels (e) and (f) are overlaid with the isophotal ellipses used to create the optical and infrared radial profiles (see § 4.1). The ellipses in panels (e) and (f) are shown as every other to be visible at this size. The red bar in panel (b) denotes a physical length of 2 kpc at the adopted distance.

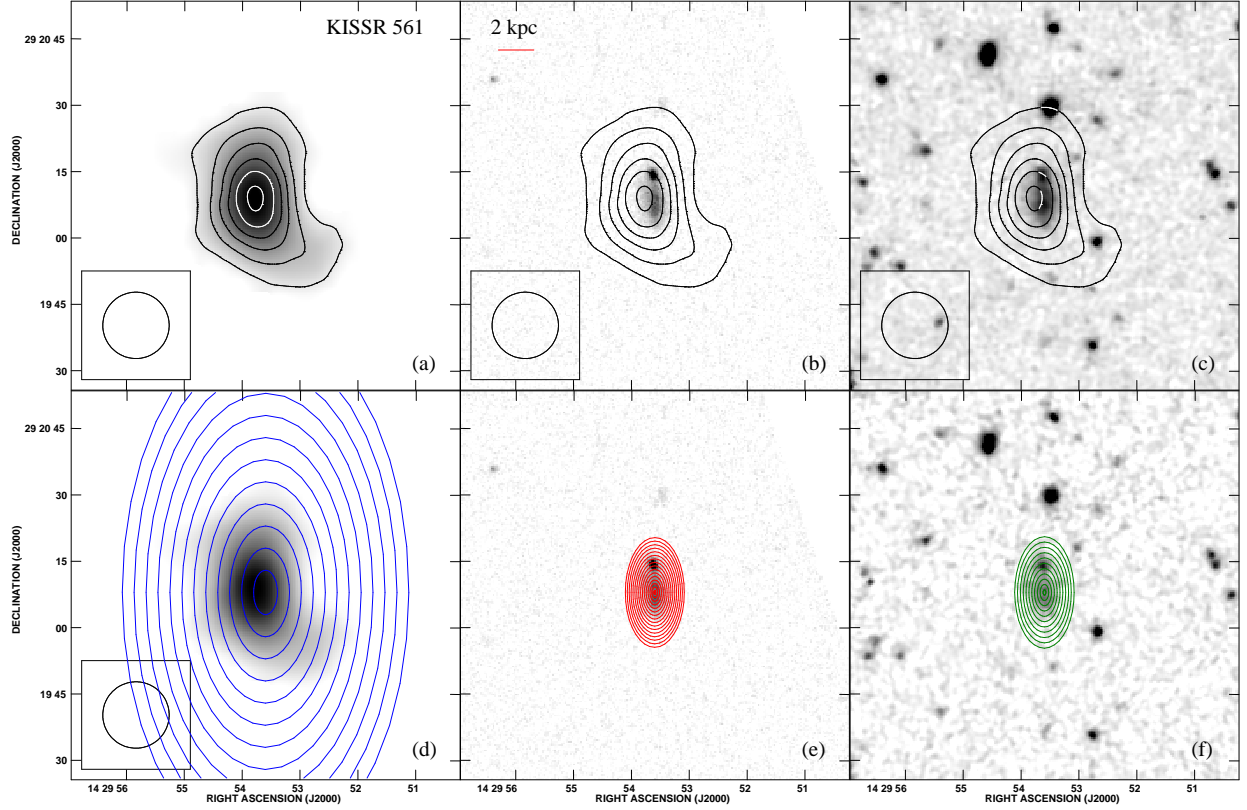


Fig. 8.— *VLA*, *SDSS* and *Spitzer* images of KISSR 561. Panels (a) and (d) show the H I column density at $15''$ resolution; panels (b) and (e) show the *SDSS* r-band image; panels (c) and (f) show the *Spitzer* $3.6\ \mu\text{m}$ (c) and $4.5\ \mu\text{m}$ (f) images. The contours in panels (a) through (c) are at the $(2, 4, 6, 8, 10, 12) \times 10^{20}\ \text{cm}^{-2}$ levels. Panel (d) is overlaid with the isophotal ellipses used to create the H I radial profile (see § 4.2), while panels (e) and (f) are overlaid with the isophotal ellipses used to create the optical and infrared radial profiles (see § 4.1). The ellipses in panels (e) and (f) are shown as every other to be visible at this size. The red bar in panel (b) denotes a physical length of 2 kpc at the adopted distance.

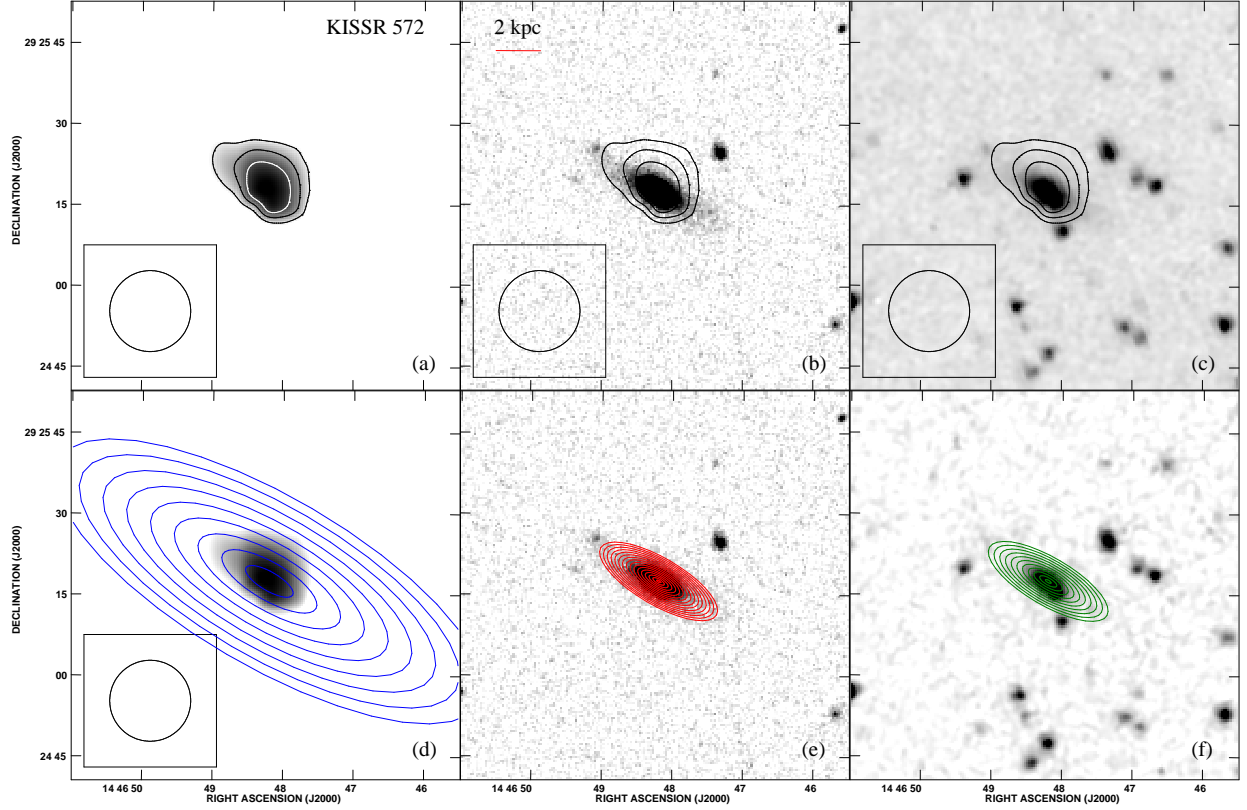


Fig. 9.— *VLA*, *SDSS* and *Spitzer* images of KISSR 572. Panels (a) and (d) show the H I column density at $15''$ resolution; panels (b) and (e) show the *SDSS* r-band image; panels (c) and (f) show the *Spitzer* $3.6 \mu\text{m}$ (c) and $4.5 \mu\text{m}$ (f) images. The contours in panels (a) through (c) are at the $(0.8, 1, 1.2) \times 10^{20} \text{ cm}^{-2}$ levels. Panel (d) is overlaid with the isophotal ellipses used to create the H I radial profile (see § 4.2), while panels (e) and (f) are overlaid with the isophotal ellipses used to create the optical and infrared radial profiles (see § 4.1). The ellipses in panels (e) and (f) are shown as every other to be visible at this size. The red bar in panel (b) denotes a physical length of 2 kpc at the adopted distance.

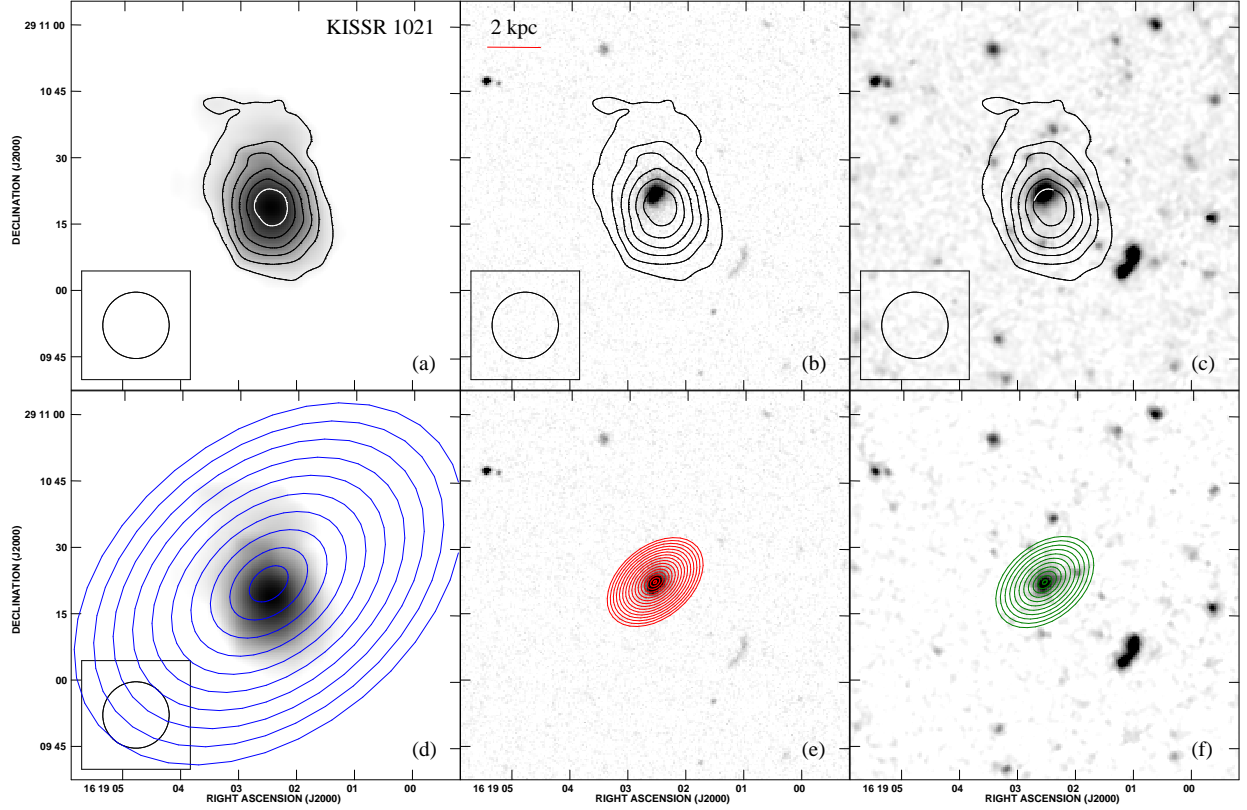


Fig. 10.— *VLA*, *SDSS* and *Spitzer* images of KISSR 1021. Panels (a) and (d) show the H I column density at $15''$ resolution; panels (b) and (e) show the *SDSS* r-band image; panels (c) and (f) show the *Spitzer* 3.6 μm (c) and 4.5 μm (f) images. The contours in panels (a) through (c) are at the $(1, 2, 3, 4, 5, 6) \times 10^{20} \text{ cm}^{-2}$ levels. Panel (d) is overlaid with the isophotal ellipses used to create the H I radial profile (see § 4.2), while panels (e) and (f) are overlaid with the isophotal ellipses used to create the optical and infrared radial profiles (see § 4.1). The ellipses in panels (e) and (f) are shown as every other to be visible at this size. The red bar in panel (b) denotes a physical length of 2 kpc at the adopted distance.

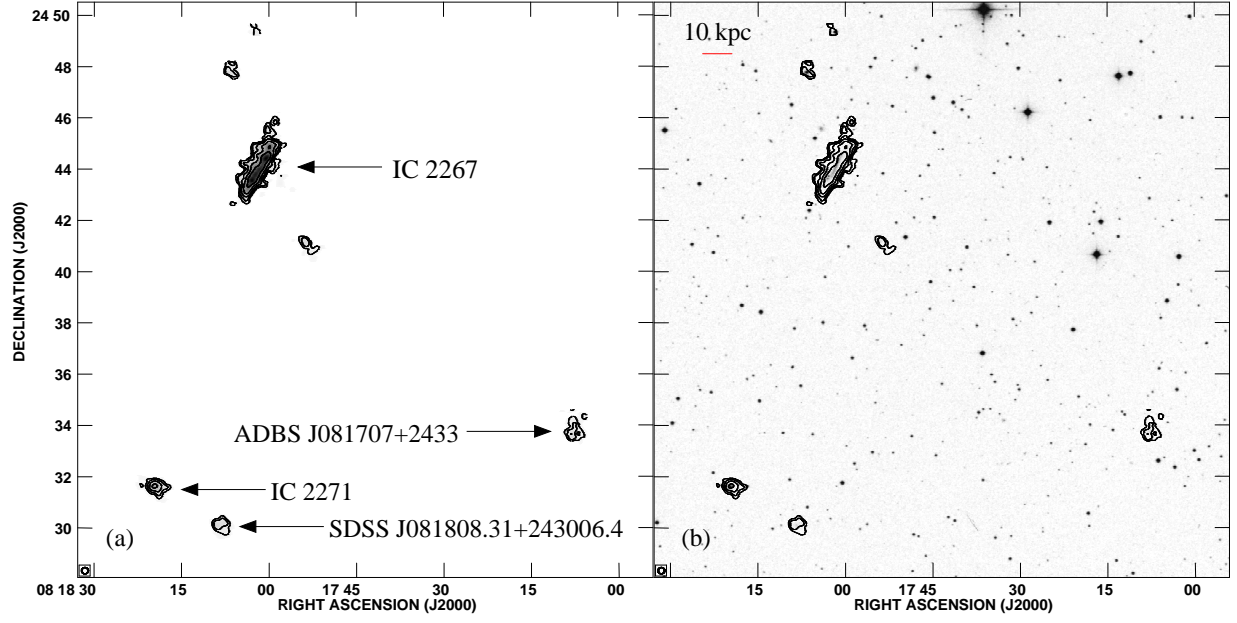


Fig. 11.— $15''$ resolution H I moment 0 (integrated H I intensity) contours over H I greyscale (a) and *Digitized Sky Survey* (DSS) r-band (b) images of the IC 2271 loose association. The contours are at levels of $(2, 4, 8, 16, 32) \times 10^{20} \text{ cm}^{-2}$. The minimum projected separations of IC 2271 and its companions are as follows: 115 kpc for IC 2267, 144 kpc for ADBS J081707+2433, and 26 kpc for SDSS J081808.31+243006.4. The red bar in panel (b) denotes a physical length of 10 kpc at the adopted distance.

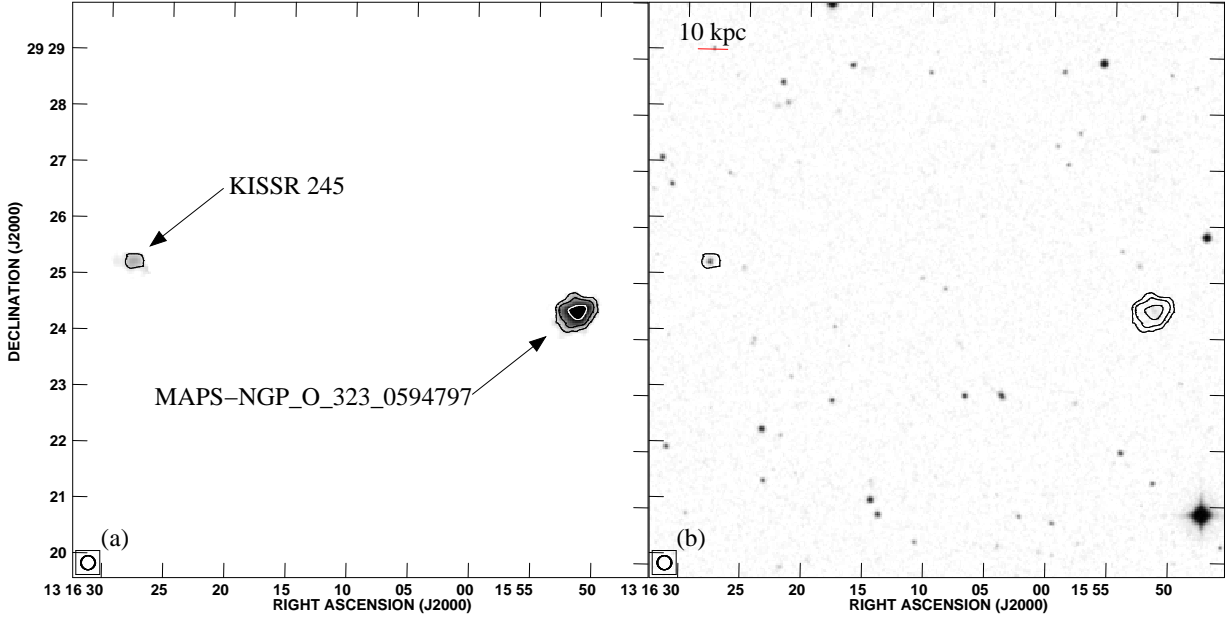


Fig. 12.— $15''$ resolution H I moment 0 (integrated H I intensity) contours over H I greyscale (a) and *DSS* r-band (b) images of the KISSR 245 loose association. The contours are at levels of $(1, 2, 4) \times 10^{20} \text{ cm}^{-2}$. The minimum projected separation of KISSR 245 and its companion (MAPS-NGP_O_323_0594797) is 151 kpc. The red bar in panel (b) denotes a physical length of 10 kpc at the adopted distance.

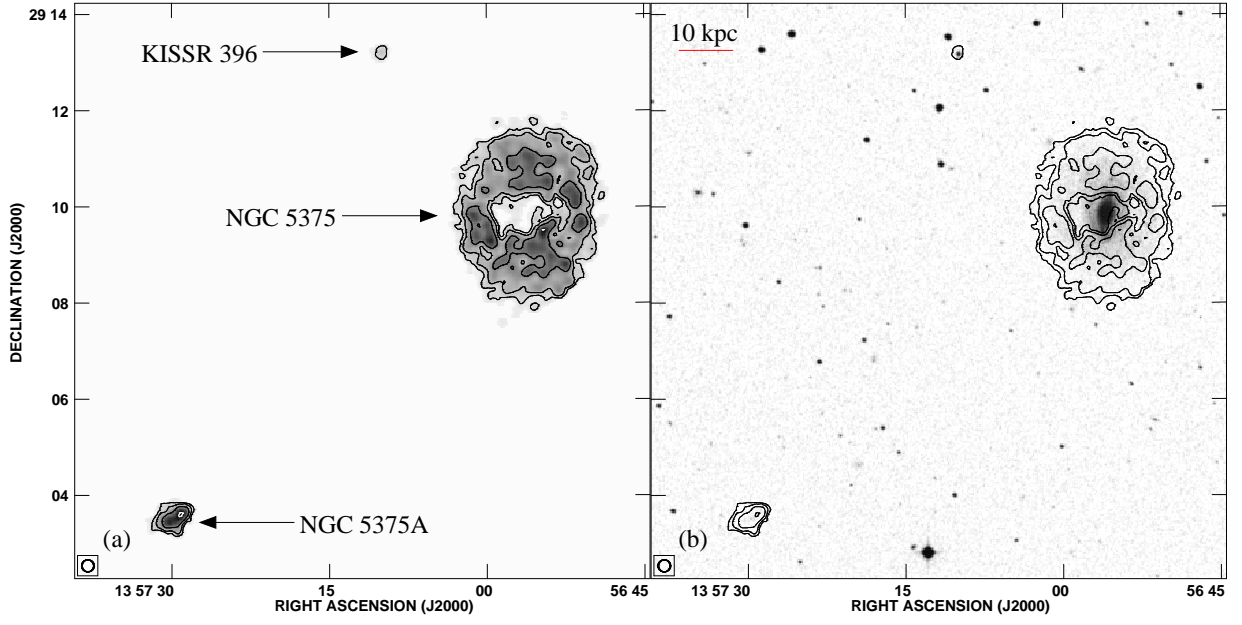


Fig. 13.— $15''$ resolution H I moment 0 (integrated H I intensity) contours over H I greyscale (a) and *DSS* r-band (b) images of the KISSR 396 loose association. The contours are at levels of $(1, 2, 4, 8) \times 10^{20} \text{ cm}^{-2}$. The minimum projected separations of KISSR 396 and its companions are as follows: 40 kpc for NGC 5657 and 94 kpc for NGC 5375A. The red bar in panel (b) denotes a physical length of 10 kpc at the adopted distance.

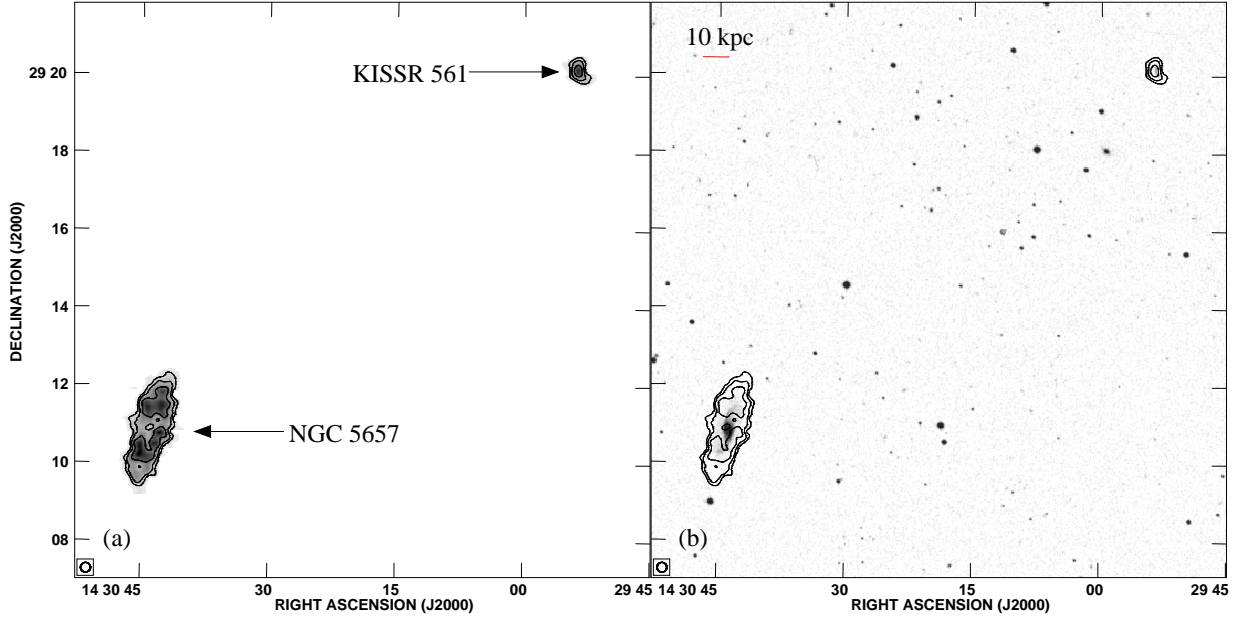


Fig. 14.— $15''$ resolution H I moment 0 (integrated H I intensity) contours over H I greyscale (a) and *DSS* r-band (b) images of the KISSR 561 loose association. The contours are at levels of $(2, 4, 8) \times 10^{20} \text{ cm}^{-2}$. The minimum projected separation of KISSR 561 and its companion (NGC 5657) is 215 kpc. The red bar in panel (b) denotes a physical length of 10 kpc at the adopted distance.

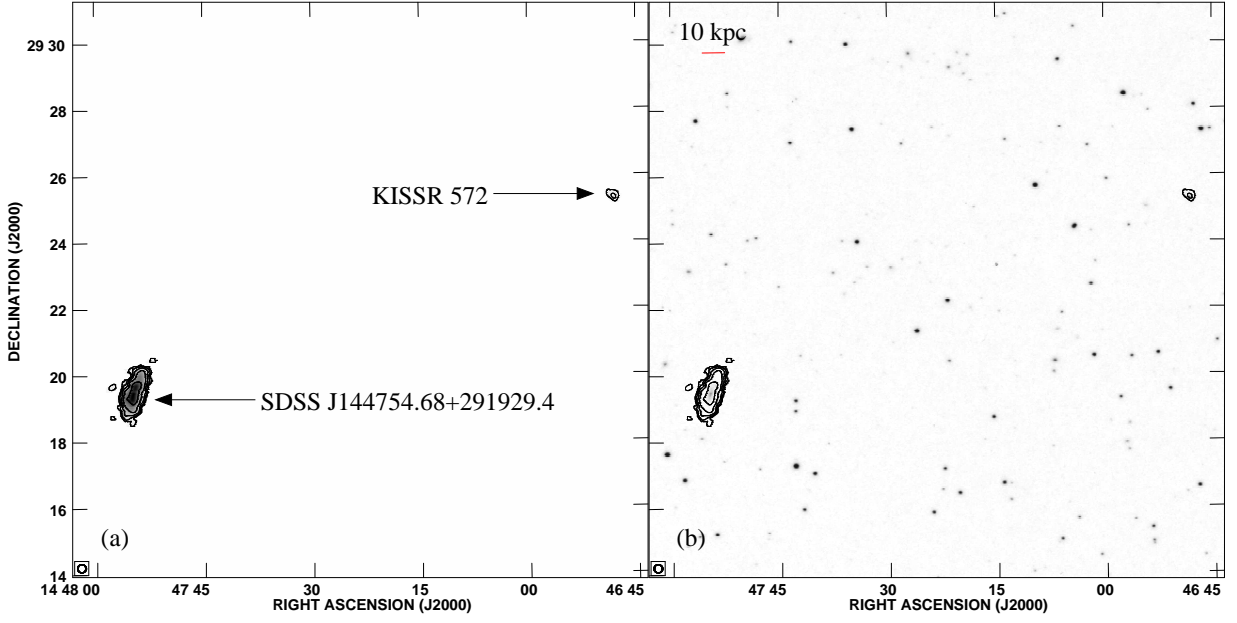


Fig. 15.— $15''$ resolution H I moment 0 (integrated H I intensity) contours over H I greyscale (a) and *DSS* r-band (b) images of the KISSR 572 loose association. The contours are at levels of $(0.6, 1.2, 2.4, 4.8, 9.6) \times 10^{20} \text{ cm}^{-2}$. The minimum projected separation of KISSR 572 and its companion (SDSS J144754.68+291929.4) is 230 kpc. The red bar in panel (b) denotes a physical length of 10 kpc at the adopted distance.

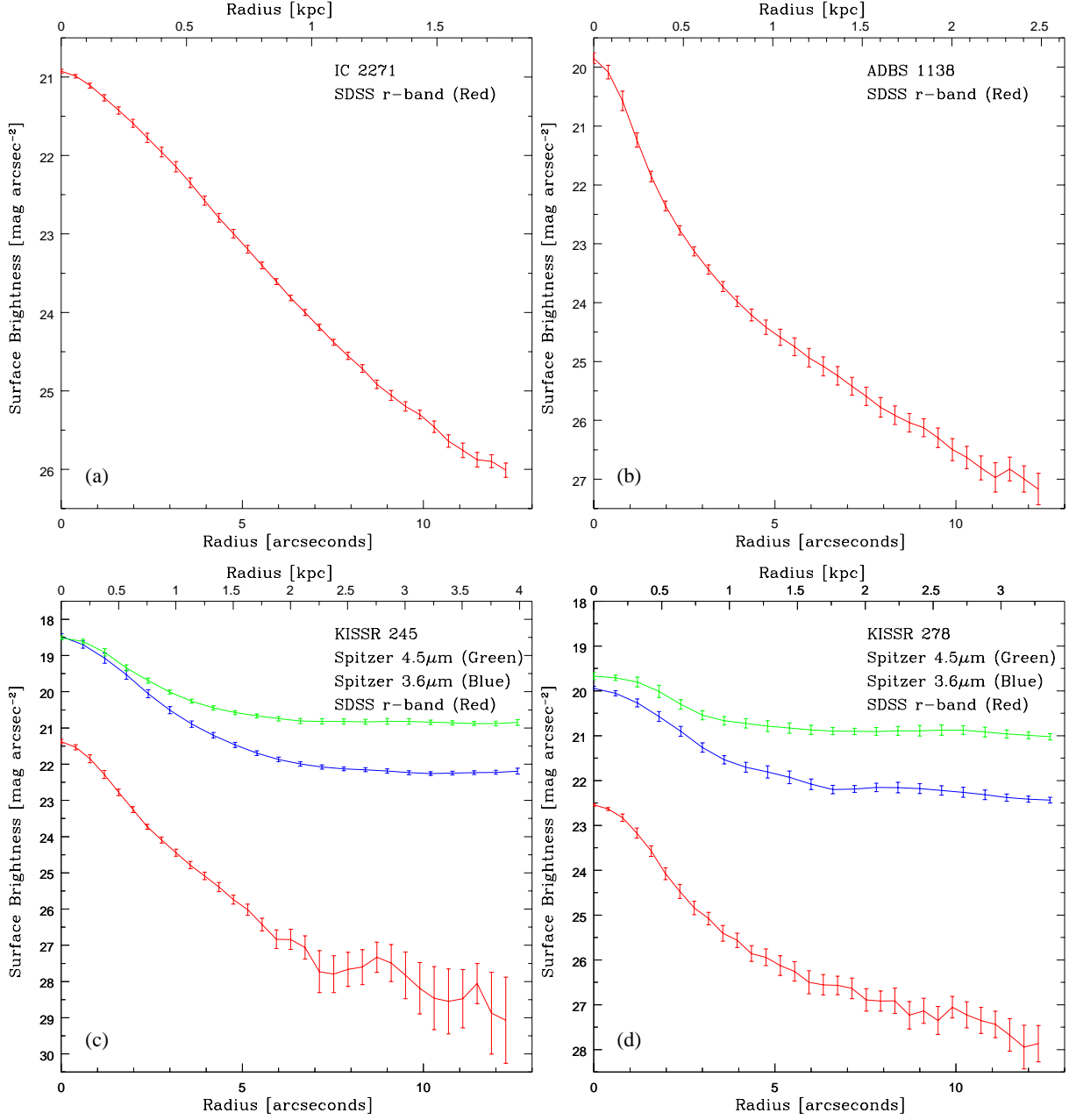


Fig. 16.— Optical and infrared surface brightness profiles of IC 2271 (a), ADBS 113845+2008 (b), KISSR 245 (c), and KISSR 278 (d). Profiles are shown in the *SDSS* r-band (red), the *Spitzer* 3.6 μ m band (blue), and the *Spitzer* 4.5 μ m band (green).

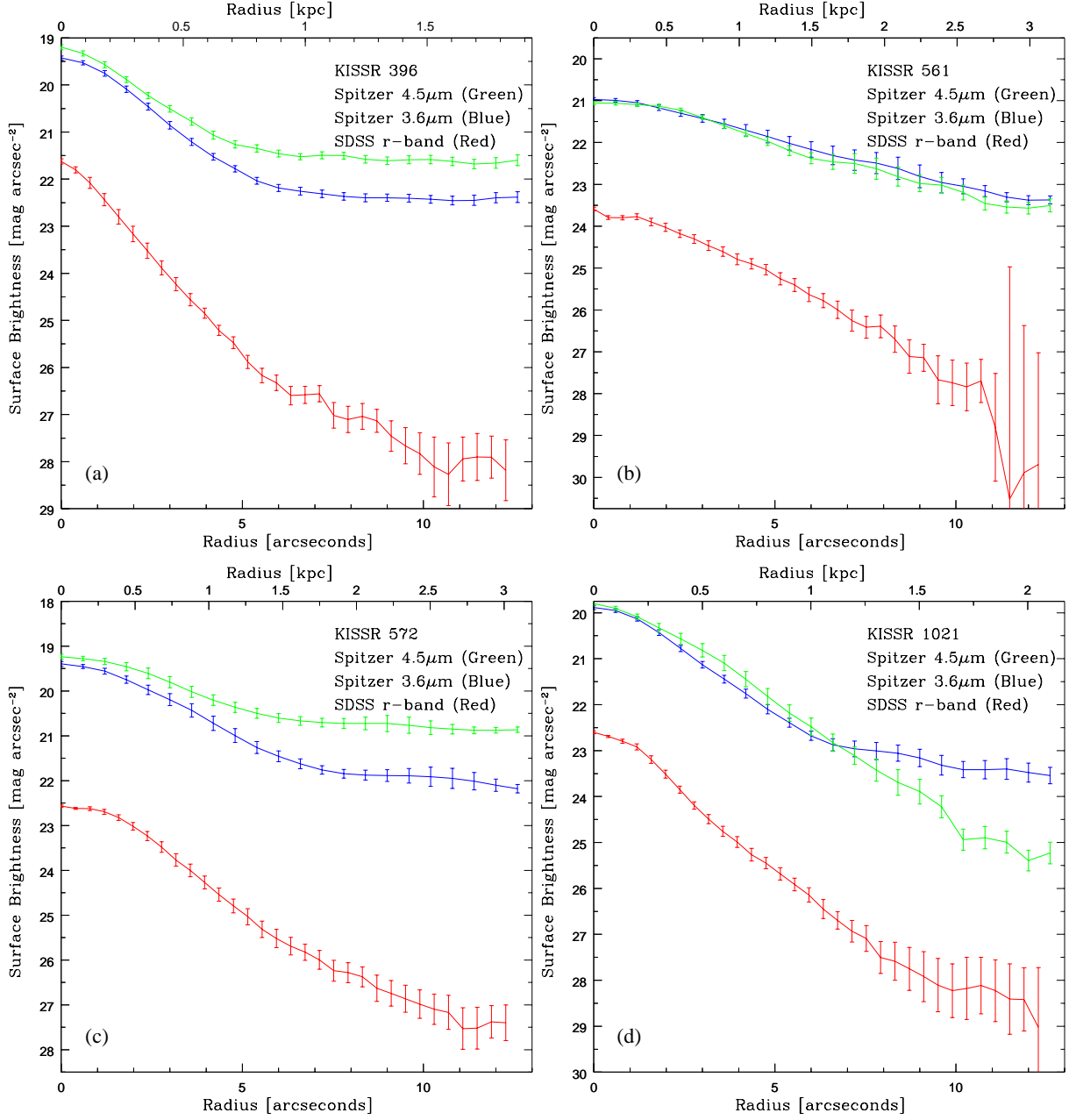


Fig. 17.— Same as Figure 16, for KISSR 396 (a), KISSR 561 (b), KISSR 572 (c), and KISSR 1021 (d).

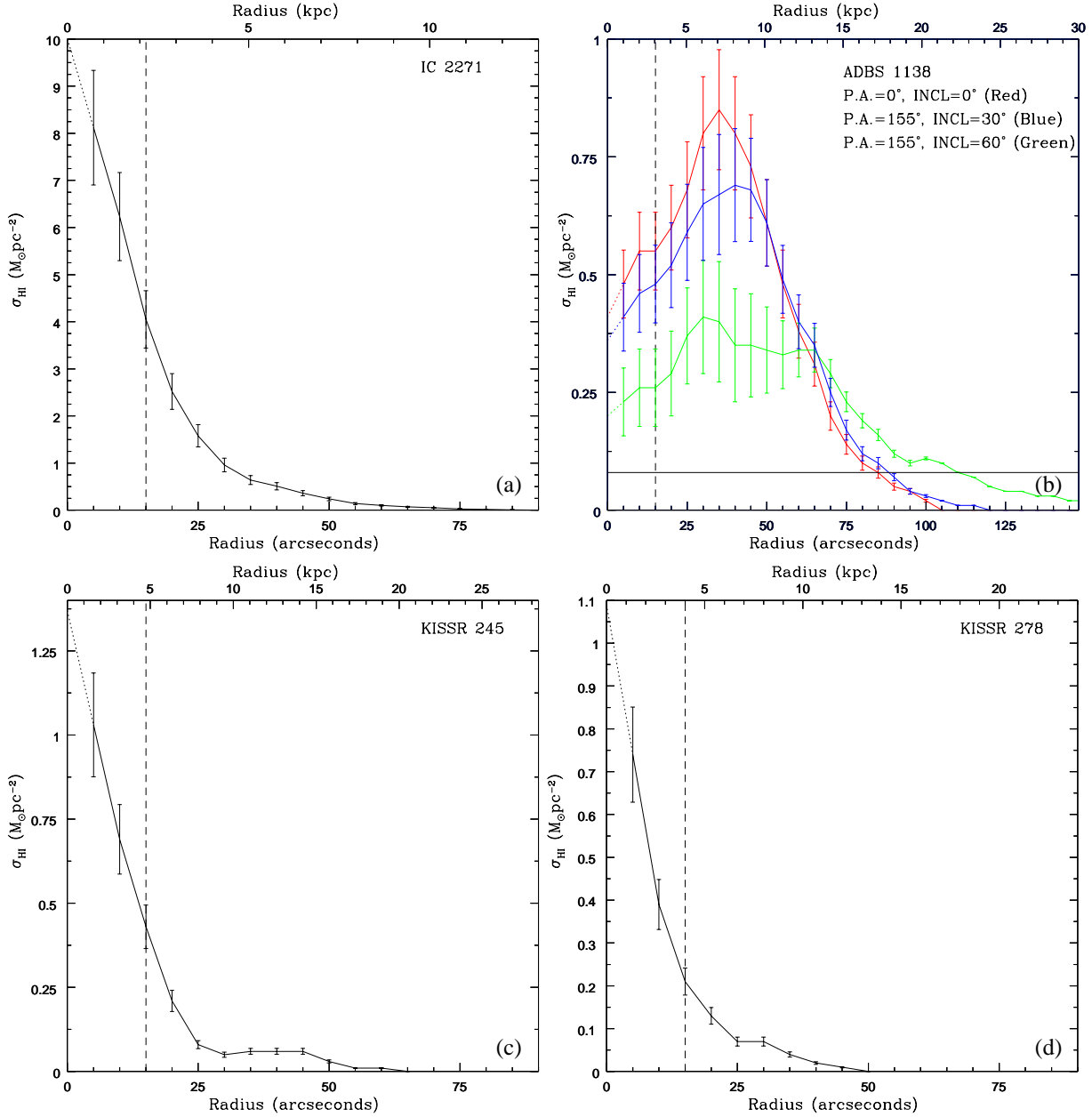


Fig. 18.— H I radial column density profiles for IC 2271 (a), ADBS 113845+2008 (b), KISSR 245 (c), and KISSR 278 (d). These profiles were created by summing the H I emission in concentric rings, with semi-major axis widths of $5''$, from the center of each of the galaxies. The vertical line denotes the H I beam size. The three profiles for ADBS 113845+2008 show fits using the *SDSS* r-band P.A. (0°) and Inclination (0°) in Red, the P.A. (155°) and Inclination (30°) from Cannon et al. (2009) in Blue, and a higher Inclination (60°) and P.A. (155°) in Green. Note the H I central depression found in the ADBS 113845+2008 profile, and that at the point of $0.08 M_{\odot} \text{pc}^{-2}$ (denoted by a horizontal line) all of the profiles are roughly equal, only becoming slightly more extended with higher inclinations.

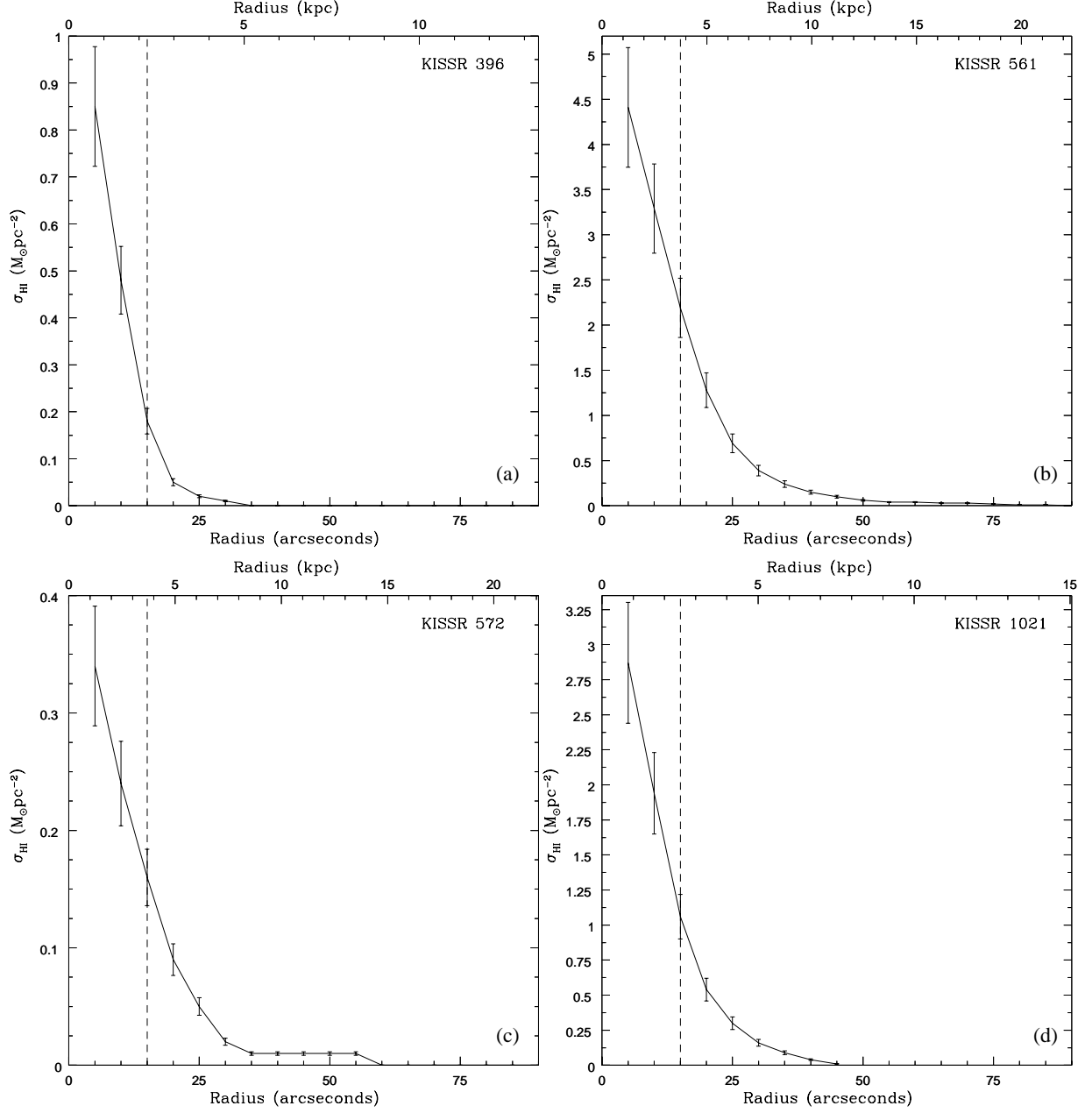


Fig. 19.— Same as Figure 18, for KISSR 396 (a), KISSR 561 (b), KISSR 572 (c), and KISSR 1021 (d). These profiles were created by summing the H I emission in concentric rings, with semi-major axis of $5''$, from the center of each of the galaxies.